



Article

Cite this article: Gkinis V, Holme C, Kahle EC, Stevens MC, Steig EJ, Vinther BM (2021). Numerical experiments on firn isotope diffusion with the Community Firn Model. *Journal of Glaciology* 67(263), 450–472. <https://doi.org/10.1017/jog.2021.1>

Received: 11 March 2020
Revised: 6 January 2021
Accepted: 6 January 2021
First published online: 10 February 2021



Keywords:

Glaciological model experiments; ice and climate; ice core; ice temperature; polar firn

Author for correspondence:

Vasileios Gkinis, E-mail: v.gkinis@nbi.ku.dk

Numerical experiments on firn isotope diffusion with the Community Firn Model

Vasileios Gkinis¹ , Christian Holme¹, Emma C. Kahle², Max C. Stevens², Eric J. Steig²  and Bo M. Vinther¹

¹Physics of Ice, Climate and Earth, Niels Bohr Institute, University of Copenhagen, Copenhagen, Denmark and ²Department of Earth and Space Sciences and Quaternary Research Centre, University of Washington, Seattle, WA, USA

Abstract

Advances in analytical methods have made it possible to obtain high-resolution water isotopic data from ice cores. Their spectral signature contains information on the diffusion process that attenuated the isotopic signal during the firn densification process. Here, we provide a tool for estimating firn-diffusion rates that builds on the Community Firn Model. Our model requires two main inputs, temperature and accumulation, and it calculates the diffusion lengths for $\delta^{17}\text{O}$, $\delta^{18}\text{O}$ and δD . Prior information on the isotopic signal of the precipitation is not a requirement. In combination with deconvolution techniques, diffusion lengths can be used in order to reconstruct the pre-diffusion isotopic signal. Furthermore, the temperature dependence of the isotope diffusion and firn densification makes the diffusion length an interesting candidate as a temperature proxy. We test the model under steady state and transient scenarios and compare four densification models. Comparisons with ice core data provide an evaluation of the four models and indicate that there are differences in their performance. Combining data-based diffusion length estimates with information on past accumulation rates and ice flow thinning, we reconstruct absolute temperatures from three Antarctic ice core sites.

Introduction

High-resolution records of the isotopic composition of polar ice cores provide a detailed picture of past climate spanning hundreds of thousands of years (Johnsen and others, 2001; EPICA Community Members, 2004, 2006; NEEM Community Members, 2013; WAIS Divide Project Members, 2015). These records carry palaeoclimatic information that can be used in order to estimate past temperatures and accumulation rates. Analytical techniques based on high throughput mass spectrometry systems, as well as laser Cavity Ring Down Spectrometry coupled to continuous melting devices (Gkinis and others, 2011; Emanuelsson and others, 2015; Jones and others, 2017b), have yielded isotopic records of very high resolution in the order of centimetres or below. In addition to their obvious potential to resolve climate signals at shorter time scales, these records open new possibilities for studies targeting the information stored in the spectral domain of the isotopic time series (Gkinis and others, 2014; Jones and others, 2018).

A well-documented example, where knowledge of the spectral signature of the isotopic time series is useful, is the characterisation of the post-depositional diffusive process that attenuates the initial isotopic signal of the precipitation, affecting particularly its high frequency bands. This diffusive process can also alter the signal to noise ratio on certain frequency bands of the $\delta^{18}\text{O}$ signal, thereby inducing a seemingly multi-decadal variability commonly measured at low accumulation Antarctic sites (Laepplé and others, 2018). Isotopic diffusion takes place first in the gas phase, within the porous medium of polar firn as it densifies and later in the ice lattice of the solid phase. The process, which has been described in theoretical as well as experimental studies (Johnsen, 1977; Cuffey and Steig, 1998; Jean-Baptiste and others, 1998; Johnsen and others, 2000; EPICA Community Members, 2006; Van der Wel and others, 2011; Gkinis and others, 2014), although seemingly detrimental to the understanding of the original isotopic signal of the deposited precipitation, can be corrected for using signal reconstruction techniques (Vinther and others, 2006, 2010; Masson-Delmotte and others, 2015; Holme and others, 2019). Moreover, due to its temperature sensitivity, the combined effect of densification and diffusion can be used in order to reconstruct past firn temperatures from polar ice cores (Gkinis and others, 2014; Holme and others, 2018).

Previous studies have focused on the problem of estimating the diffusion length quantity σ , a parameter that is equal to the mean vertical displacement of a water molecule due to diffusion. It is thus related to the amount of smoothing the isotopic signal has undergone in the firn and can be estimated from the power spectral density of high-resolution isotopic records (Gkinis and others, 2014; Jones and others, 2017a; Holme and others, 2018; Kahle and others, 2018). Holme and others (2018) have shown how to utilise the (obtained) diffusion length signal in order to estimate past firn temperatures using various techniques and compared their estimates to modern day temperatures for several deep ice core sites.

These comparisons indicate that the diffusion technique can yield reliable estimates of past temperatures. Such reconstructions are useful for the study of the temperature evolution in

© The Author(s), 2021. Published by Cambridge University Press. This is an Open Access article, distributed under the terms of the Creative Commons Attribution licence (<http://creativecommons.org/licenses/by/4.0/>), which permits unrestricted re-use, distribution, and reproduction in any medium, provided the original work is properly cited.

Greenland during the deglaciation and the Holocene epoch (Buizert and others, 2014; Gkinis and others, 2014) as well as for the study of the response of the Greenland ice sheet to the Holocene optimum signal (Nielsen and others, 2018). In the aforementioned studies, a simple, steady-state Herron and Langway (1980) firn-densification model is used in combination with the analytical solution of the diffusion length σ (for a complete list of the symbols used throughout the manuscript the reader is referred to Table 6).

The densification of polar firn into ice plays an important role in the process of water-isotope diffusion in firn. The porous medium of the firn provides the space wherein water vapour molecular transport takes place. The rate at which firn densifies into ice is temperature and accumulation dependent, whereas the upper and lower boundaries of the diffusion process are determined by the surface snow density at the top and the depth at which the firn is dense enough so that the diffusive fluxes cease.

In this study, we use the Community Firn Model (CFM) (Stevens, 2018), which comprises various densification models and additional tools for modelling the firn diffusion of atmospheric gases. We built a fork of the CFM called Iso-CFM that contains modules for the calculation of the diffusion length as a function of depth for the full firn column. Using two main input variables, surface temperature and accumulation, Iso-CFM calculates the diffusion length profiles of the HD¹⁶O, H₂¹⁸O and H₂¹⁷O isotopologues, while it offers the possibility to modify several other physical parameters related to the densification and diffusion processes. We note that the calculated diffusion lengths are not dependent on the isotopic composition of ice itself, hence Iso-CFM does not require any input information on the $\delta^{18}\text{O}$ signal.

We test the Iso-CFM for a range of conditions under steady-state and transient scenarios using temperature and accumulation forcing parameters close to those met at ice core drilling sites in Greenland and Antarctica. The Iso-CFM module includes a root-finding inversion tool that allows for the calculation of past surface temperatures given a value for the diffusion length and the accumulation rate. Depending on the study case, other inversion techniques can be applied using more complex approaches such as least-squares, Bayesian or Monte-Carlo methods. Using our simple inversion routine we provide uncertainty estimates for temperature estimations based on the results of different densification models and diffusion length data from three ice core sites. We focus our study on four densification models that have been used in the past for ice core studies. These are the following:

- (1) The dynamic version of the Herron and Langway model in its two different parameterisations (Herron and Langway, 1980), noted as HLD and HLS.
- (2) Barnola densification model (Barnola and others, 1991), noted as BAR.
- (3) Goujon densification model (Goujon and others, 2003), noted as GOU.

Methods

Vapour diffusion of water isotopes in polar firn

Diffusive exchange of water isotopes in firn is a process that takes place from the time of deposition until pore close-off and can be described by Fick's second law. For present conditions and typical deep ice core sites in Greenland and Antarctica this range spans approximately the top 50–80 m of firn. The bottom layer of this column has an age of ≈ 200 –300 years for the case of the Greenlandic sites and can be as old as 2500–3000 years in the case of low accumulation, cold sites in East Antarctica (Buizert and others, 2013). Accounting for the vertical strain rate, the

differential equation describing the process is (Johnsen and others, 2000; Gkinis and others, 2014; Holme and others, 2018):

$$\frac{\partial \delta}{\partial t} = \frac{\partial}{\partial z} \left(D(t, z) \frac{\partial \delta}{\partial z} \right) - \dot{\epsilon}_z(t) z \frac{\partial \delta}{\partial z} \quad (1)$$

The $\delta(z, t)$ notation (isotopic abundances are reported as deviations of a sample's isotopic ratio relative to that of a reference water (e.g. VSMOW) expressed in per mil as: $\delta^i = (R_{\text{sample}}/R_{\text{SMOW}} - 1) \times 1000$ where ${}^2R = {}^2\text{H}/{}^1\text{H}$ and ${}^{18}R = {}^{18}\text{O}/{}^{16}\text{O}$) refers to the isotopic composition of the polar firn as a function of time t and the vertical coordinate z . Here, $D(t)$ is the diffusivity coefficient (variables dependent on z are also dependent on t . However, in some equations we omit one of the two dependent variables for more clarity). For our application, $D(t)$ does not account only for molecular Fickian diffusive transport in the porous firn medium. It also incorporates the phase transitions as well as the isotopic fractionation effects involved in the process (for more details, the reader is referred to Section 'Implementation of the firn diffusivity'). Our treatment of diffusion here, does not take into account possible mixing due to convective fluxes at the top of the firn column. $\dot{\epsilon}_z(t)$ is the vertical strain rate due to firn densification. A solution to Eqn (1) can be given by the convolution of the initial isotopic profile δ_0 with a Gaussian filter \mathcal{G} (Johnsen, 1977; Kreyszig, 2006):

$$\delta(z) = S(z) [\delta_0(z) * \mathcal{G}(z)] \quad (2)$$

where \mathcal{G} is the Gaussian filter with SD σ equal to:

$$\mathcal{G}(z) = \frac{1}{\sigma\sqrt{2\pi}} e^{-z^2/2\sigma^2}, \quad (3)$$

and S is the total thinning of the layer at depth z equal to:

$$S(z) = e^{\int_0^z \dot{\epsilon}_z(z') dz'}. \quad (4)$$

Equation (4) applies for any depth between the surface and the bottom of the ice core and S refers to total thinning due to ice compaction and firn densification. In the case of Iso-CFM our main interest is the firn column where ice compaction can be considered negligible, hence S refers only to thinning due to firn densification. Omitting the ice flow thinning, the convolution operation in Eqn (2) yields a quantitative description of the amplitude decay of a harmonic with wavelength λ and initial amplitude Γ_0 as (Gkinis and others, 2014; Kahle and others, 2018):

$$\Gamma = \Gamma_0 e^{-2(\pi\sigma/\lambda)^2}. \quad (5)$$

The key parameter in our description is the SD term σ , a measure of the amount of diffusive smoothing a layer undergoes. Also referred to as the diffusion length, σ depends on the diffusivity coefficient and the vertical strain rate (Johnsen, 1977; Gkinis and others, 2014):

$$\frac{d\sigma^2}{dt} - 2\dot{\epsilon}_z(t)\sigma^2 = 2D(t). \quad (6)$$

For the case of firn and assuming a site with modest ice flow, we can approximate the vertical strain rate with the firn densification rate as:

$$\dot{\epsilon}_z(t) \approx -\frac{d\rho}{dt} \frac{1}{\rho}, \quad (7)$$

where ρ is the firn density (the expression in Eqn (7) can be obtained by making the assumption that an annual layer of firn sinks vertically a distance equal to its own thickness and combining it with a mass balance equation). Combining Eqns (6) and (7) we obtain a differential equation for the diffusion length σ that depends on firn density and the diffusivity coefficient:

$$\frac{d\sigma^2}{dt} + 2 \frac{\sigma^2}{\rho} \frac{d\rho}{dt} = 2D(t). \tag{8}$$

From Eqn (8) we see that the calculation of the diffusion length σ depends primarily on the accuracy of the firn densification and diffusivity parameterisations. Another notable point is that the calculation does not take into account any information on the mean value, nor on the variability of the $\delta^{18}\text{O}$ signal in the firn/ice. Therefore, estimating the diffusive effects on the isotopic signal for an ice core site does not require any prior measurements of $\delta^{18}\text{O}$. Combined with an already diffused $\delta^{18}\text{O}$ time series, Iso-CFM can be used as a tool to reconstruct the pre-diffusion signal.

The Community Firn Model

The CFM is an open-source firn-model framework. It is coded in Python and available on GitHub (Stevens and others, 2020). The CFM is designed to be modular, meaning (1) the user can easily control which physical processes (or modules) are included in a model run and (2) additional modules can be easily integrated. The CFM’s core modules simulate the evolution of firn density and temperature on a Lagrangian (parcel-following) grid (Fig. 1). During each time step in the model, the densification rate is provided by any one of a number of previously published firn-densification models, and the firn density is updated explicitly at each time step. Then, heat diffusion is calculated using a fully-implicit, finite-volume method (Patankar, 1980). A new layer with properties provided by the model input (temperature, density, and mass) is added to at the top of the grid and the bottom layer is removed. The model’s vertical domain is typically kept at 200–300 m depth and the influence of the warmer temperatures close to the bedrock is omitted as negligible. A comprehensive description of the model can be found in Stevens (2018) and Stevens and others (2020).

Implementation of the firn diffusivity

Within Iso-CFM, we provide a specific module for the calculation of the diffusivity $D(\rho)$ (see computation flow diagram in Fig. 1). It contains several methods for the calculation of the various parameters involved in the diffusivity coefficient. For some of these parameters, options for various parameterisations are also available. The diffusivity parameterisation follows the formulation from Johnsen and others (2000)

$$D(z) = \frac{m p D_{ai}}{R T(z) \alpha_{s/v}^i \tau(z)} \left(\frac{1}{\rho(z)} - \frac{1}{\rho_{ice}} \right). \tag{9}$$

The terms used in Eqn (9) and their parameterisations are outlined in Table 6 and described in detail below:

- m*: molecular weight (kg)
- p*: saturation vapour pressure over ice (Pa)

There are two different options for the calculation of p based on Murphy and Koop (2005) as:

$$p = \exp\left(28.9074 - \frac{6143.7}{T}\right) \tag{10}$$

$$p = \exp\left(9.5504 - \frac{5723.265}{T} + 3.530 \ln(T) - 0.0073 T\right) \tag{11}$$

The difference between Eqns (10) and (11) is that the latter takes into account the temperature dependence of the latent heat of sublimation of ice when integrating the Clausius–Clapeyron equation. A third expression for p is given by (Johnsen and others, 2000):

$$p = 3.454 \times 10^{12} \exp\left(\frac{-6133}{T}\right). \tag{12}$$

We use Eqn (12) for our calculations hereafter. Based on tests we have performed, the three different parameterisations of p yield very similar results for the range of temperatures we work with.

D_a: Diffusivity of water vapour in air ($m^2 s^{-1}$)

We use (Hall and Pruppacher, 1976):

$$D_a = 2.1 \times 10^{-5} \left(\frac{T}{T_o}\right)^{1.94} \left(\frac{P_o}{P}\right) \tag{13}$$

with $P_o = 1$ Atm, $T_o = 273.15$ K and P, T the ambient pressure (Atm) and temperature (K). Additionally from Merlivat (1978) $D_{a^{2H}} = D_a/1.0251$ and $D_{a^{18O}} = D_a/1.0285$.

R: Molar gas constant $R = 8.314478$ ($m^3 Pa K^{-1} mol^{-1}$)

T: Ambient temperature (K)

$\alpha_{s/v}^i$: Solid–vapour fractionation factor.

For $\alpha_{s/v}^{18}$ there is an option to choose between the fractionation factor parameterisation from Majoube (1971) or from Ellehøj and others (2013) respectively, given by:

$$\ln \alpha_{s/v}^{18} = \frac{11.839}{T} - 28.224 \times 10^{-3} \tag{14}$$

and

$$\ln \alpha_{s/v}^{18} = 0.0831 - \frac{49.192}{T} + \frac{8312.5}{T^2}. \tag{15}$$

For the case of $\alpha_{s/v}^2$ the parameterisation from Merlivat and Nief (1967), Ellehøj and others (2013) or Lamb and others (2017) can be chosen as:

$$\ln \alpha_{s/v}^2 = \frac{16288}{T^2} - 9.45 \times 10^{-2} \tag{16}$$

or

$$\ln \alpha_{s/v}^2 = 0.2133 - \frac{-203.1}{T} + \frac{48888}{T^2} \tag{17}$$

or

$$\ln \alpha_{s/v}^2 = \frac{13525}{T^2} - 5.59 \times 10^{-2} \tag{18}$$

respectively. For $\alpha_{s/v}^{17}$ we use $\alpha_{s/v}^{17} = 0.529 \alpha_{s/v}^{18}$ based on Barkan and Luz (2005). In Section ‘The influence of the fractionation factor parameterisation’ we present a comparison of the different parameterisations. Majoube (1971) and Merlivat and Nief (1967) are the default choices and are also used throughout the rest of the paper.

τ : Firn tortuosity

We use (Johnsen and others, 2000):

$$\frac{1}{\tau} = \begin{cases} 1 - b_\tau \left(\frac{\rho}{\rho_{ice}}\right)^2 & \rho \leq \frac{\rho_{ice}}{\sqrt{b_\tau}} \\ 0 & \rho > \frac{\rho_{ice}}{\sqrt{b_\tau}} \end{cases} \tag{19}$$

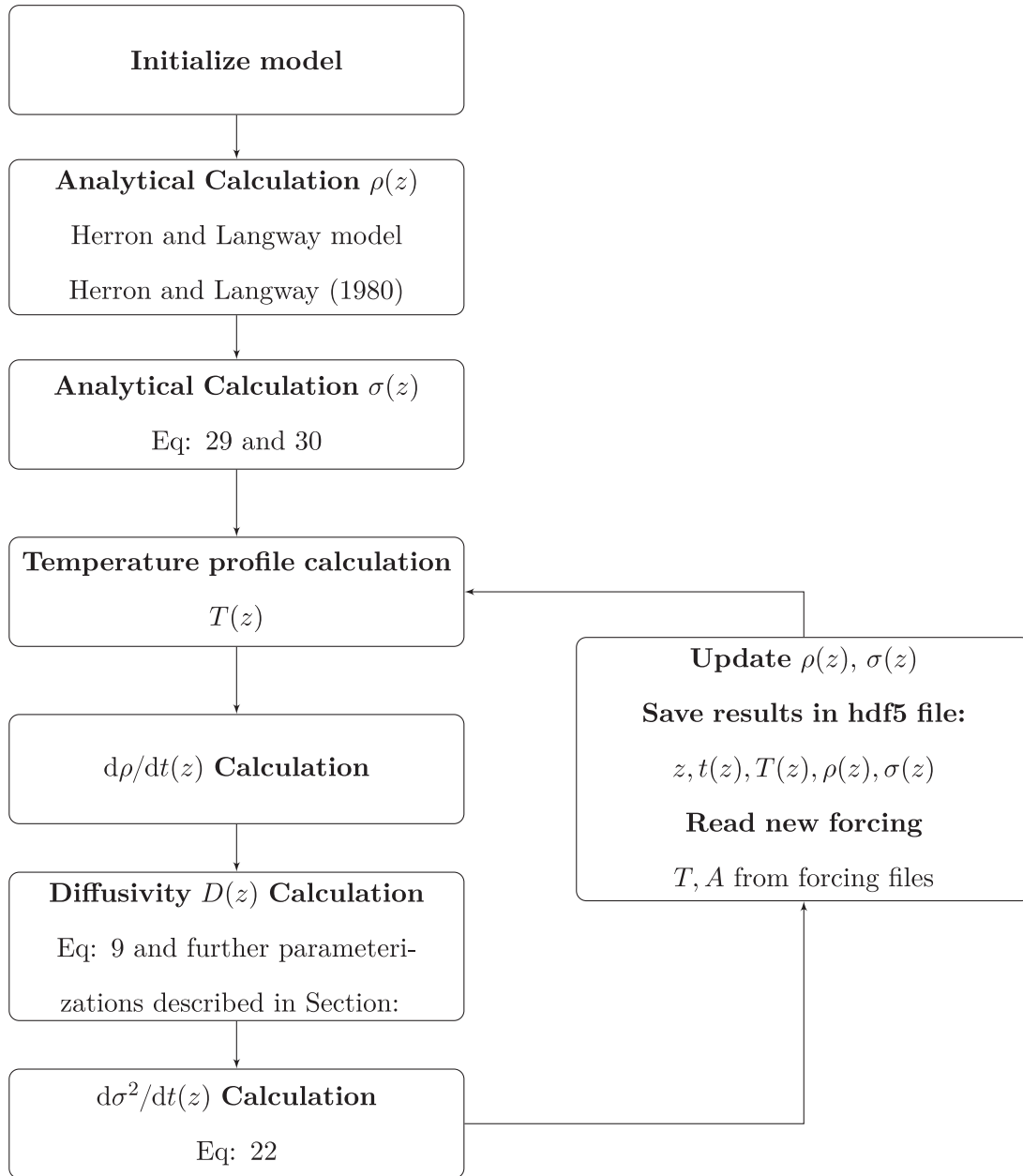


Fig. 1. Computation flow diagram of the Iso-CFM model.

where $b_\tau = 1.3$ and $\rho_{ice} = 917 \text{ kg m}^{-3}$ implying a close-off density of $\rho_{co} = 804.3 \text{ kg m}^{-3}$ for $1/\tau = 0$. Equation (19) is based on the diffusivity laboratory experiments by Schwander and others (1988) that are also supported by results from the experimental study by Jean-Baptiste and others (1998). The value of the close-off density that we use here, refers to the depth at which the diffusive fluxes stop and the ratio between the diffusivity in air and the effective diffusivity $D_a/D_{eff} \rightarrow \infty$.

Another expression for the tortuosity implemented in Iso-CFM that yields very similar results with Eqn (19) is from Schwander (1989):

$$\frac{1}{\tau} = 1.7(s - s_{cl}) - 0.2 \tag{20}$$

where s is the total porosity ($= 1 - \rho/\rho_{ice}$) and s_{cl} the closed porosity which in Schwander (1989) follows an empirical relationship as:

$$s_{cl} = \begin{cases} s \exp\left[75\left(\frac{\rho}{830} - 1\right)\right] & 0 \leq \rho \leq 830 \text{ kg m}^{-3} \\ s & \rho > 830 \text{ kg m}^{-3} \end{cases} \tag{21}$$

Ice core diffusion length profiles

Numerical and analytical solutions for σ

In Iso-CFM, we follow the original time-stepping scheme of the CFM (Fig. 1). For each iteration j , using the output of CFM for $d\rho/dt$, ρ and T we calculate the quantity $d\sigma^2/dt$ as:

$$\frac{d\sigma^2}{dt} = 2\left(D(t) - \frac{\sigma^2}{\rho} \frac{d\rho}{dt}\right) \tag{22}$$

In Figure 2, we plot the three terms of Eqn (22) as well as the diffusion length value that is the result of the numerical integration of Eqn (22). The forcing we use is $T = 242 \text{ K}$ and $A = 0.131 \text{ m a}^{-1}$ ice eq. and we implement the HLD model. As seen in Figure 2, the diffusion length signal is a result of two opposing processes, on one hand the positive contribution of the isotope firm diffusivity ($2D(t)$, dot line in Fig. 2) and on the other hand the negative contribution of the densification process (term $\frac{-2\sigma^2}{\rho} \frac{d\rho}{dt}$, dot-dash line in Fig. 2). The diffusivity term $2D(t)$ is positive at all times

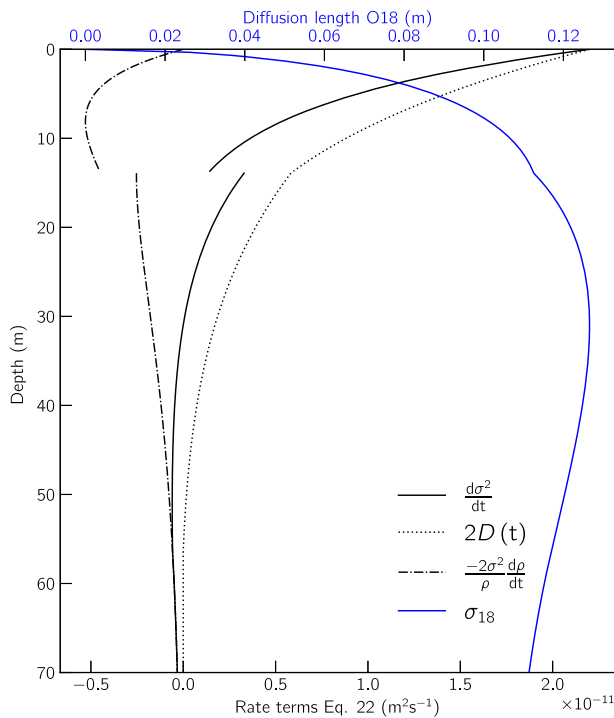


Fig. 2. Contribution of the diffusion and densification terms (Eqn 22) on the evolution of the diffusion length signal as a function of depth.

and decreases from the surface and until the close-off depth where it is equal to zero. Note how at depths below ≈ 30 m in our calculation the densification term dominates over the diffusion term and thus $d\sigma^2/dt$ is negative and the value of the diffusion length is decreasing. Note also the discontinuities on both rate terms at ≈ 15 m. These are due to the transition zone of the HLD model at the critical density of 550 kg m^{-3} described by the two activation energies in Eqns (26) and (27).

For the initial iteration of the model, we calculate the diffusion length profile using analytical equations derived from Eqn (8). Calculations based on these analytical equations have previously been shown in Johnsen and others (2000); Gkinis and others (2014) and Holme and others (2018). However, to our knowledge the equations themselves have not been published. Therefore, we present them here with a short description of their derivation. Rearrangement and substitution of variables in Eqn (8) results in:

$$\frac{d\sigma^2}{d\rho} + \frac{2\sigma^2}{\rho} = 2 \left(\frac{d\rho}{dt} \right)^{-1} D(\rho). \tag{23}$$

The latter can be converted into the integral form:

$$\sigma^2(\rho) = \frac{1}{\rho^2} \int_{\rho_0}^{\rho} 2\rho^2 \left(\frac{d\rho}{dt} \right)^{-1} D(\rho) d\rho. \tag{24}$$

We use the densification rate parameterisation from Herron and Langway (1980):

$$\frac{d\rho(z)}{dt} = k(T)A^\vartheta(\rho_{\text{ice}} - \rho(z)), \tag{25}$$

where $k(T)$ is a temperature-dependent Arrhenius-type densification rate coefficient described by:

$$k_0(T) = 0.011 \exp\left(-\frac{10160}{RT}\right), \vartheta = 1, \quad \rho < 550 \text{ kg m}^{-3}, \tag{26}$$

and

$$k_1(T) = 0.575 \exp\left(-\frac{21400}{RT}\right), \vartheta = 0.5, \quad \rho \geq 550 \text{ kg m}^{-3}. \tag{27}$$

Using the diffusivity coefficient from Johnsen and others (2000) (the quantities involved in the calculation of the diffusivity coefficient are described in detail in Section ‘Implementation of the firn diffusivity’) and substituting the fraction term in front of the parentheses with Ξ

$$D(\rho) = \frac{\Xi}{RT\alpha_i} \left(1 - \frac{1.3\rho^2}{\rho_{\text{ice}}^2}\right) \left(\frac{1}{\rho} - \frac{1}{\rho_{\text{ice}}}\right) \tag{28}$$

we finally obtain the analytical equations for the diffusion length σ for the sections above and below the critical density $\rho_c = 550 \text{ kg m}^{-3}$:

$$\sigma^2(\rho < \rho_c) = \frac{\Xi}{\rho^2 k_o A \rho_{\text{ice}}} \left[\rho^2 - \rho_o^2 - \frac{1.3}{2\rho_{\text{ice}}^2} (\rho^4 - \rho_o^4) \right] \tag{29}$$

$$\begin{aligned} \sigma^2(\rho \geq \rho_c) &= \frac{\Xi}{\rho^2 k_1 A^{0.5} \rho_{\text{ice}}} \left[\rho^2 - \rho_c^2 - \frac{1.3}{2\rho_{\text{ice}}^2} (\rho^4 - \rho_c^4) \right] \\ &+ \frac{\Xi}{\rho^2 k_o A \rho_{\text{ice}}} \left[\rho_c^2 - \rho_o^2 - \frac{1.3}{2\rho_{\text{ice}}^2} (\rho_c^4 - \rho_o^4) \right] \end{aligned} \tag{30}$$

Iso-CFM calculates both the analytical solution of the diffusion length, as well as the time derivative $d\sigma^2/dt$ from Eqn (22).

Contour of analytical solutions for the diffusion length at the close-off density

Based on Eqn (30) we calculate the diffusion length value at the close-off density for H_2^{18}O using a broad range of temperature-accumulation rate combinations. Hereafter we use the prime notation σ'_{18} to denote the diffusion length value at the close-off depth. The calculation results in a contour plot (Fig. 3) that (a) allows the estimation of the expected diffusion length value for a number of ice coring sites and (b) provides an overview of the uncertainties expected in reconstructing temperatures based on a diffusion length value. It is apparent that an uncertainty of 1 cm for the diffusion length value σ'_{18} results in different uncertainties in temperature. As seen in the contour plot, at the accumulation level of 0.1 m a^{-1} ice eq. a σ'_{18} uncertainty of 1 cm results in a temperature uncertainty of $\approx 5 \text{ K}$ for temperatures around 220 K and of $\approx 2 \text{ K}$ for temperatures around 240 K. This is an auxiliary plot to some of the diffusion length uncertainty calculations following in the paper.

Steady-state experiments

Steady-state climate forcing

We run two experiments using steady-state climate forcing. For both experiments, the model is spun up for 1000 years, and the main model run lasts 400 years. The model domain is set to 300 m and heat diffusion is enabled. The first experiment (A), consists of 30 model runs, each with a unique temperature and accumulation rate pairing. Following previous studies (Johnsen and others, 1995; Dahl Jensen and others, 1998), we assume a logarithmic relationship between the forcing temperature and

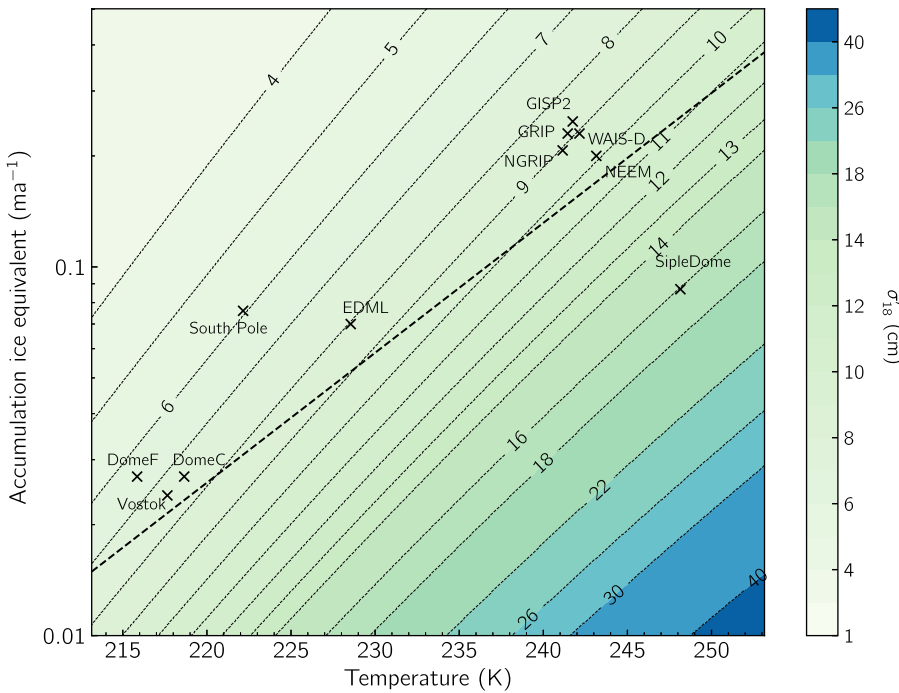


Fig. 3. Contour map of analytical solutions for σ'_{18} expressed in cm of firm eq. at the density of ρ_{co} . For all the calculations $P = 0.7 \text{ Atm}$, $\rho_o = 350 \text{ kg m}^{-3}$, $\rho_{co} = 804.3 \text{ kg m}^{-3}$. The dash straight line represents the temperature-accumulation forcing of the steady-state experiments as described by Eqn (31).

accumulation. The temperatures range linearly in the range 213–250 K, and the accumulation rates follow a natural logarithm relationship described as:

$$\ln A = -21.492 + 0.0811 T \tag{31}$$

Equation (31) describes a temperature–accumulation relationship that should be seen as qualitative only and not necessarily as representative of actual ice sheet conditions.

The temperature–accumulation forcing is shown in Figure 4. For experiment A we use annual time steps. Experiment B consists of seven runs for which we force the model using monthly time steps with a seasonal temperature cycle (Thompson, 1969; Lundin and others, 2017):

$$T = T_{amp}(\cos(2\pi t) + 0.3 \cos(4\pi t)) \tag{32}$$

where $T_{amp} = 10 \text{ K}$. Note that no seasonality is assumed for the accumulation, which remains constant at its mean annual value. The accumulation–rate temperature pairs for experiment B are shown as pink diamonds in Figure 4.

For every run, diffusion length profiles for $\delta^{17}\text{O}$, $\delta^{18}\text{O}$ and δD are calculated. In Figure 5 we present the diffusion length value for each isotopologue at the close-off depth ($\rho_{co} = 804.3 \text{ kg m}^{-3}$) expressed in m of firm (vertical distance) and symbolised with the primed notation as σ'_D , σ'_{18} and σ'_{17} . We also include the calculations for the close-off depth. For the specific temperature–accumulation relationship we use here (Eqn 4), it is clearly seen that the effect of the increasing temperature is dominating by increasing the diffusion length value and shifting the close-off depth further up. For the first effect, the driving mechanism is the firm and air diffusivity as described in Eqns (9) and (13). The higher densification rates resulting in a shallower close-off depth can be explained by the temperature dependence of the densification rates which in the case of the HLD and HLS are given in Eqns (26) and (27). The BAR and GOU models use similar relationships although with different activation energies. The increase in accumulation rate results in a more effective ‘sealing’ between the layers thus reducing the isotopic gradients and

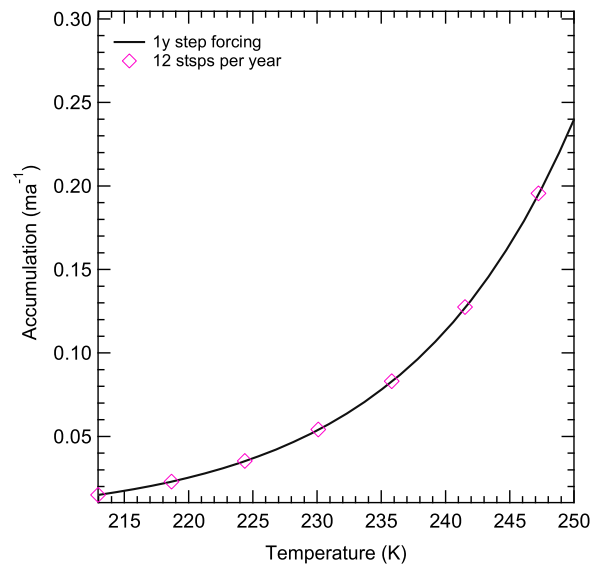


Fig. 4. Steady-state T and A forcing for experiments A and B. The pink markers indicate the mean forcing for experiment B for which temperature a seasonal cycle with an amplitude of 10 K is enabled.

hence hindering diffusion. Additionally, higher accumulation values result in a deeper close-off depth and as a result allow for a diffusion process that lasts longer in time. These two effects of the accumulation increase are not visible in this experiment due to the temperature dominating the process. For a better insight in the separate effects of temperature and accumulation on the value of the diffusion length, we refer the reader to Sections ‘Ramp experiments’, ‘Warming pulse experiments’ and Figures 12, 20 and 21.

Overall, the results of experiment A indicate a very good agreement between the HLD, HLS and BAR model whereas the GOU model deviates from the rest of the models in the range of higher forcing temperatures/accumulations. Specifically, as the temperature reaches values close to 250 K, the discrepancy is in the order of $\approx 1 \text{ cm}$ for σ'_{18} (similar for σ'_{17} and σ'_D). As far as

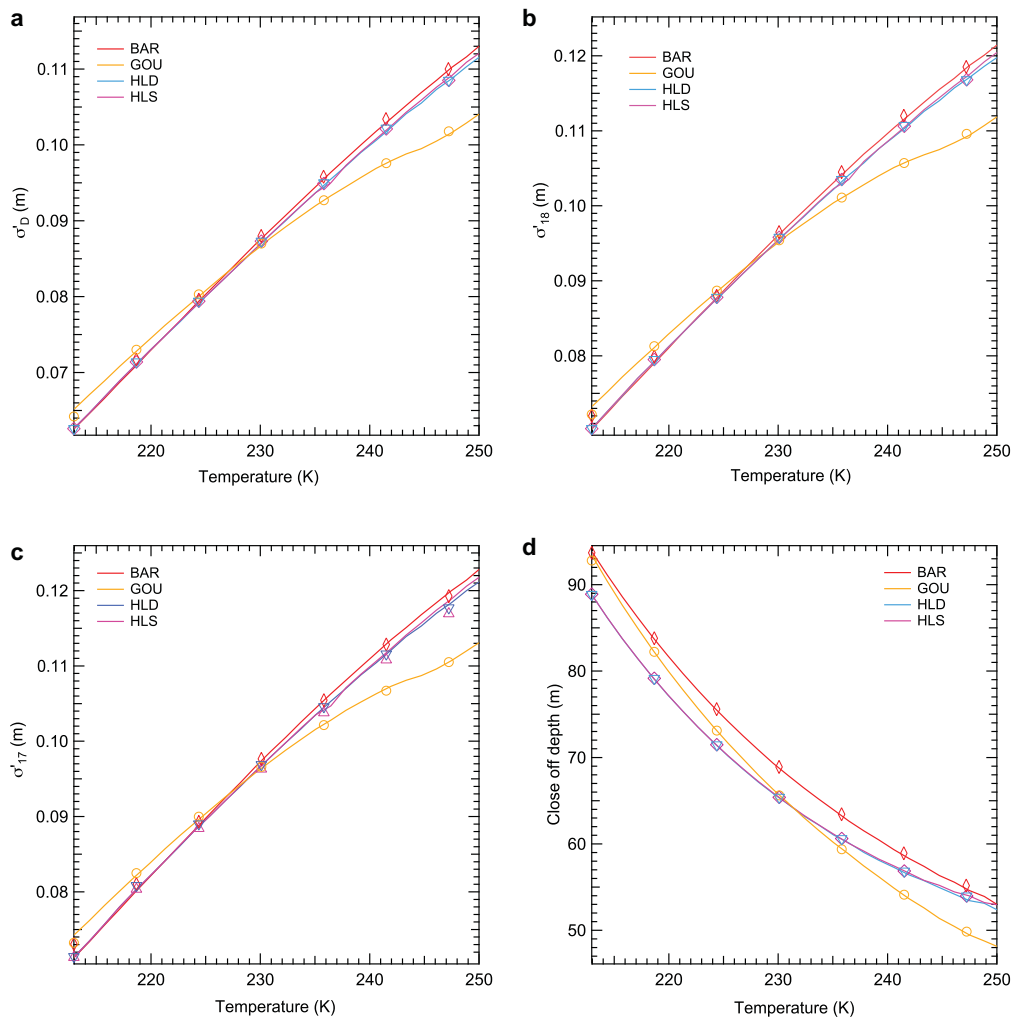


Fig. 5. Results of model runs using steady-state forcing with and without temperature seasonal cycle enabled. Solid lines (markers) represent runs with the temperature seasonal cycle disabled (enabled). The prime notation for the diffusion length σ' represents the value of the diffusion length at the close-off depth ($\rho = 804.3 \text{ kg m}^{-3}$) and expressed in m of firn.

the seasonal temperature signal is concerned, we observe a minimal influence of the annual cycle on the results with an effect that is more profound for the case of the GOU model. In Figure 22 in the Appendix, we give a more detailed view of the temperature and diffusion length signals with and without seasonality.

The influence of the fractionation factor parameterisation

We investigate the influence of the parameterisation used for the fractionation factor $\alpha_{s/v}^i$ by performing a test identical to experiment A and by using the various expressions presented here for $\alpha_{s/v}^i$ (Eqns 14–18). As seen from Figure 6, the calculated discrepancies are minimal. A notable exception is that of the Ellehøj and others (2013) parameterisation for deuterium that seems to yield a higher (although still not significant) deviation from the results obtained using the Merlivat and Nief (1967) and Lamb and others (2017) relations. Based on the good agreement between the experiments of the two latter studies, we choose to use the Merlivat and Nief (1967) and Majoube (1971) parameterisations throughout the paper.

Diffusion length profiles

We present (Fig. 7) density and diffusion length profiles for the last time step of the model (year 400) for two sets of climate forcing regimes. The first one (type 1) is roughly representative of

conditions of the East Antarctic Plateau ($T_1 = 222.66 \text{ K}$, $A_1 = 0.031 \text{ m a}^{-1} \text{ ice eq.}$) and the second (type 2) is more representative of conditions of ice coring sites on the Greenland ice sheet ($T_2 = 242 \text{ K}$, $A_2 = 0.131 \text{ m a}^{-1} \text{ ice eq.}$) (Table 1).

First, we note the good agreement between the H–L type models. The two dynamic implementations (HLD and HLS) and the analytical H–L model yield very similar results for all the diffusion length and density calculations. This is not a surprising result, considering that all three implementations are variations of the same model. However, as we show later, the dynamic response of these three implementations can be rather different. Second, there is a significant discrepancy between the GOU and the rest of the models for the type 2 regime (warmer conditions). This discrepancy is in line with the results of Section ‘Steady-state climate forcing’.

The lower diffusion length values of the GOU implementation for the type 2 forcing can be explained by the higher densification rates predicted by this model for the full span of the firn column. Similarly, the BAR model densifies faster than the HLS and HLD models for the upper part of the firn. However, for densities in the range $\approx 600\text{--}800 \text{ kg m}^{-3}$, the H–L-type models predict higher densification rates. The net effect is that the three models yield very similar values for the diffusion length at the close-off depth. This indicates that both the upper ($< 550 \text{ kg m}^{-3}$) and the lower stages ($> 550 \text{ kg m}^{-3}$) of the densification play an important role in the diffusion process.

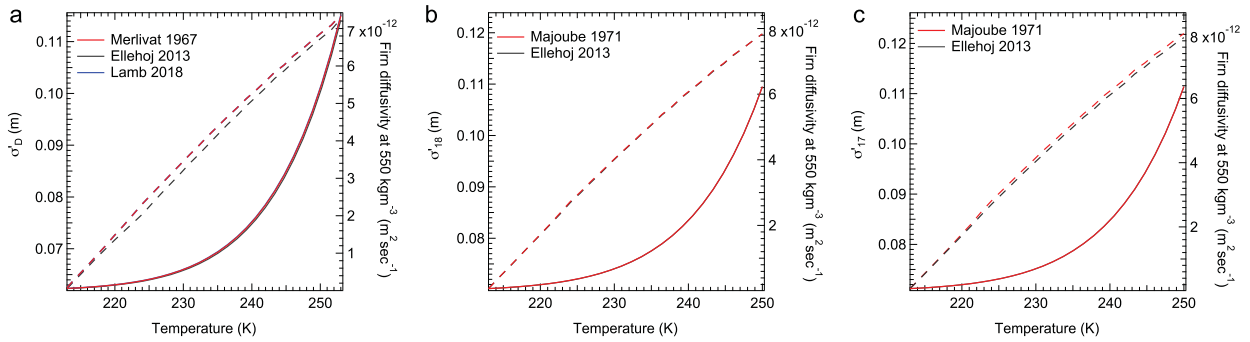


Fig. 6. Estimation of the diffusion length value σ' at the close-off depth (dash lines) and the firm diffusivity for the density $\rho_c = 550 \text{ kg m}^{-3}$ (solid lines) with various parameterisations of the fractionation factor $\alpha'_{s/v}$. For the plots where there appears only one curve per parameter, the lines are visually indistinguishable from each other.

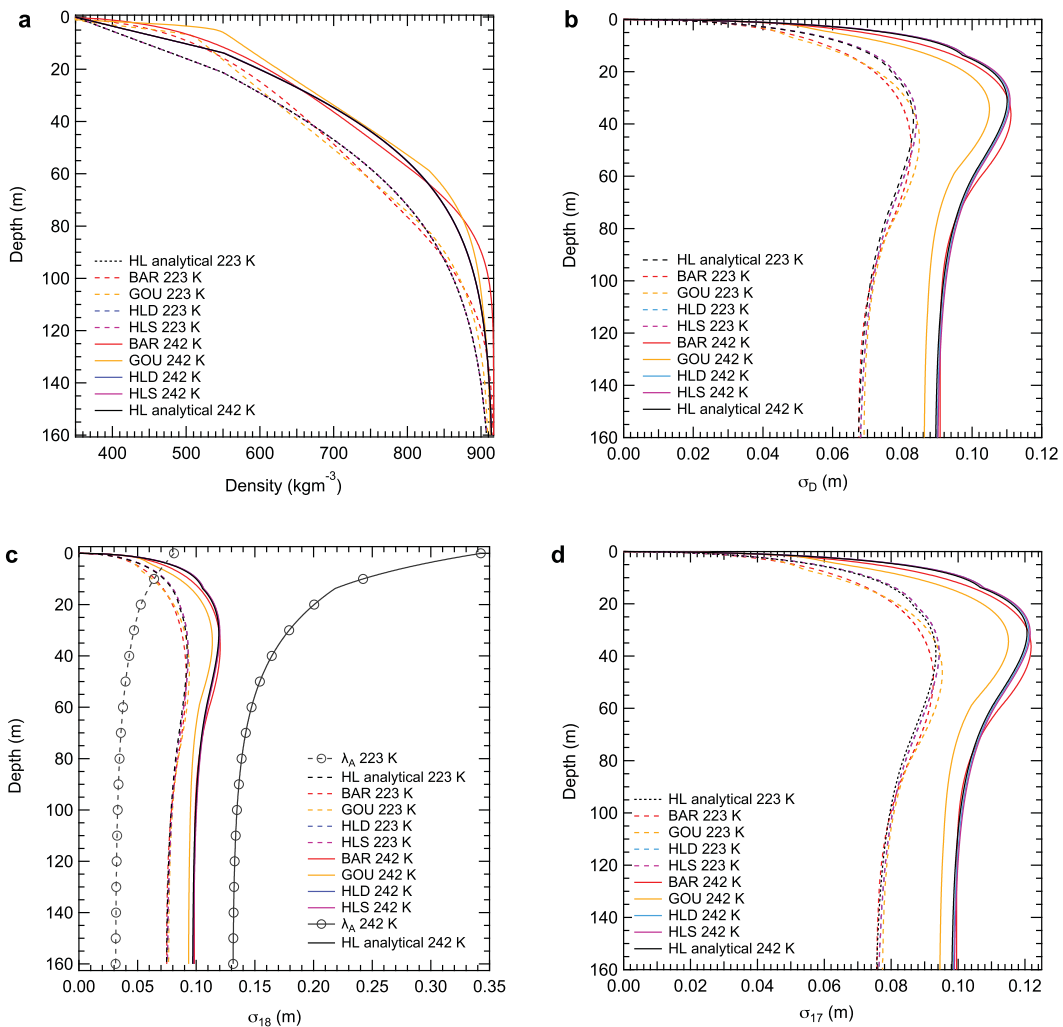


Fig. 7. Firm density and diffusion length profiles for type 1 (dash lines) and type 2 (solid lines) steady-state climate forcing. In (c) we also plot the annual layer thickness λ_A deduced from the density profile using the HLD model.

As seen in Figure 7, for type 1 conditions the diffusion length is higher than the annual layer thickness throughout the whole firm column, thus obliterating the annual cycle. For the higher accumulation rates of the type 2 climate forcing we should expect

a better ‘sealing’ of the adjacent firm isotopic layers, effectively hindering diffusive transport. However, it is apparent that the temperature of the firm column plays a dominant role in the formation of the σ_{18} signal resulting in higher diffusion length values.

Table 1. Type 1 and type 2 climate forcing regimes

Type 1	$T_1 = 222.66 \text{ K}$	$A_1 = 0.031 \text{ m a}^{-1}$
Type 2	$T_2 = 242 \text{ K}$	$A_2 = 0.131 \text{ m a}^{-1}$

Close-off density and the tortuosity factor

The value of the close-off density ρ_{co} signifies the point at which $1/\tau \rightarrow 0$ and thus $D = 0$ (Eqn 9). At this point the diffusive fluxes

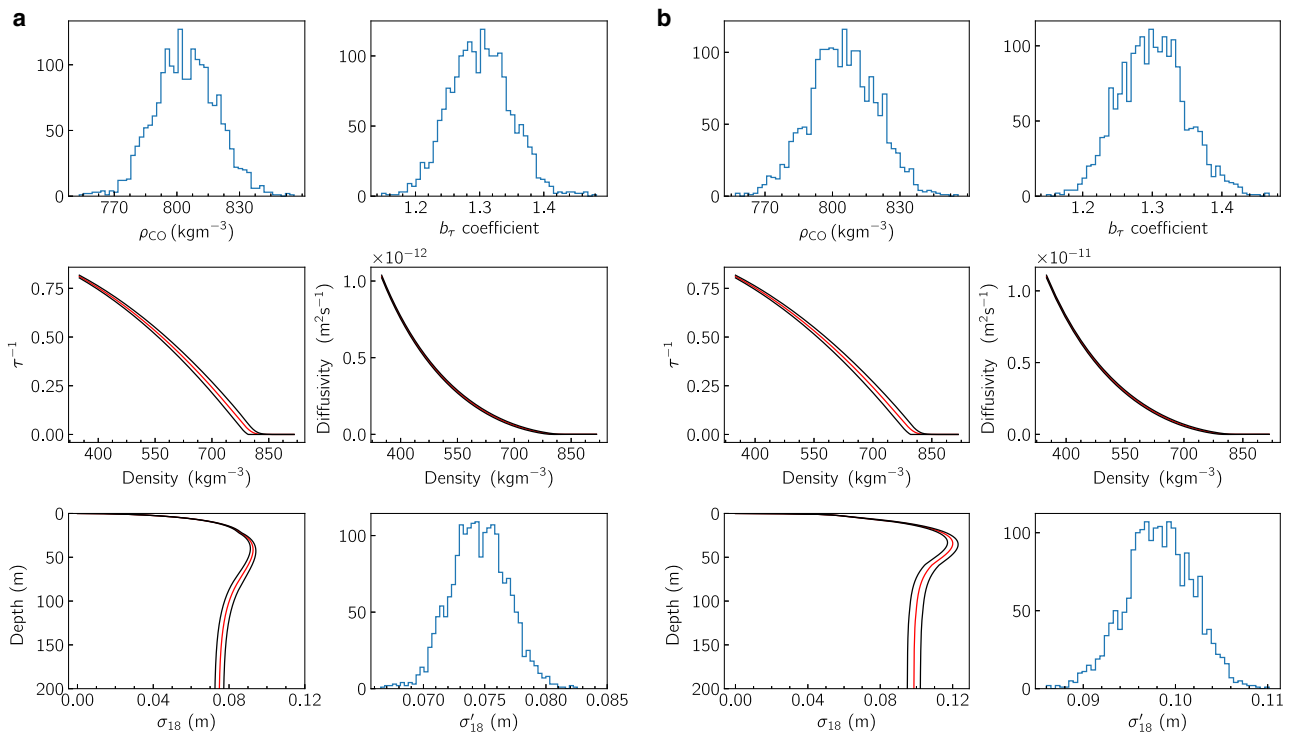


Fig. 8. (a) Type 1 climate forcing. (b) Type 2 climate forcing. Close-off density/tortuosity sensitivity test. 2000 repetitions with $\rho_{co} = 804.3 \pm 15 \text{ kg m}^{-3}$. The HLD densification model is used for the test. The 1-standard deviation intervals of inverse tortuosity, the diffusivity and the diffusion length are represented by the black lines while the red lines represent the mean profiles of these quantities. The values of σ'_{18} are given in m ice eq. and 'b coefficient' refers to the tortuosity scaling factor b_τ as given in Eqn (19) and Table 6.

seize and the process of vapour diffusion terminates. Commonly, in gas-diffusion firn studies the term 'full close-off depth' refers to the depth at which the open porosity of the firn reaches the value of zero and hence the bubbles are occluded (Martinerie and others, 1992). Typical values for the full close-off density are $\approx 830 \text{ kg m}^{-3}$. Despite the risk of confusing these two different terms we will use the term 'close-off depth' and 'close-off density' in order to be compatible with previous studies on water isotope firn diffusion.

The empirical form for $1/\tau$ (Eqn 19) is based on laboratory measurements of the diffusivity. The majority of the measurements are performed for the CO_2 and O_2 gases using real firn core sections (Schwander and others, 1988). In the study of Jean-Baptiste and others (1998), diffusivity coefficients were estimated by measuring the concentration changes along HDO gradients in artificial ice in the range of densities $\approx 580\text{--}800 \text{ kg m}^{-3}$. The measurements presented in that study are consistent with a close-off density for the diffusive fluxes equal to $\approx 800\text{--}805 \text{ kg m}^{-3}$. However due to the lack of data covering the range of the lower densities we perform here a sensitivity test investigating the influence of the tortuosity uncertainty on the diffusion length value for type 1 and type 2 climate forcing regimes.

In the Iso-CFM it is possible to adjust the value of ρ_{co} . This in turn results in modifying the value of the scaling parameter b_τ in Eqn (19) such that $1 - b_\tau(\rho_{co}/\rho_{ice}) = 0$. We perform 2000 repetitions of a steady-state run using the HLD model where the ρ_{co} value is drawn from a normal distribution with a mean of 804.3 kg m^{-3} and a SD of 15 kg m^{-3} . We ran the experiment for the type 1 and type 2 climate forcing regimes. The resulting diffusion length distributions (σ'_{18}) are presented in m of ice eq. (Fig. 8). Based on the results of the calculation the uncertainty (1-SD) on the diffusion length is $\approx \pm 0.0025 \text{ m}$ for type 1 and \pm

0.0034 m for the type 2 climate forcing (Fig. 8). Moreover, the influence of the varying close-off density and thus the tortuosity profile is increasingly more important with increasing depth. Based on the contour plot of Figure 3 the resulting uncertainty with respect to temperature is also similar for both climate forcing regimes and equal to $\approx 1 \text{ K}$. The test indicates the importance of the tortuosity profile and its impact on the diffusivity coefficient and diffusion length profiles.

Influence of the amplitude of the temperature seasonal cycle

To investigate the influence of the amplitude of the temperature seasonal cycle, we perform an experiment where we run all four implementations of the model for type 1 and type 2 conditions, for a range of values of the T_{amp} parameter in Eqn (32). We vary T_{amp} in the range $[0, 14] \text{ K}$ with a step of 1 K . For the case of type 1 conditions, we perform a spin-up run of 1000 years and a main run of 2000 years, while for the type 2 regime the spin-up and main runs are 500 years long each.

As seen in Figure 9, the influence of the T_{amp} parameter on the value of σ'_D , σ'_{18} and σ'_{17} is apparent, although minimal, while the value of the diffusion length increases with T_{amp} due to the nonlinear dependence of the diffusivity coefficient to temperature. The difference between diffusion lengths in the $T_{amp} = 0 \text{ K}$ and $T_{amp} = 14 \text{ K}$ runs is on the order of $5 \times 10^{-4} \text{ m}$ for all models and all diffusion lengths, translating to a temperature difference in the order of mK. Additionally, all four models behave similarly for both type 1 and type 2 conditions. For the GOU model we note that for the type 2 (higher temperature and accumulation) conditions, its deviation is higher than the other three models, a finding that is in line with the previous Sections 'Steady-state climate forcing' and 'Diffusion length profiles'.

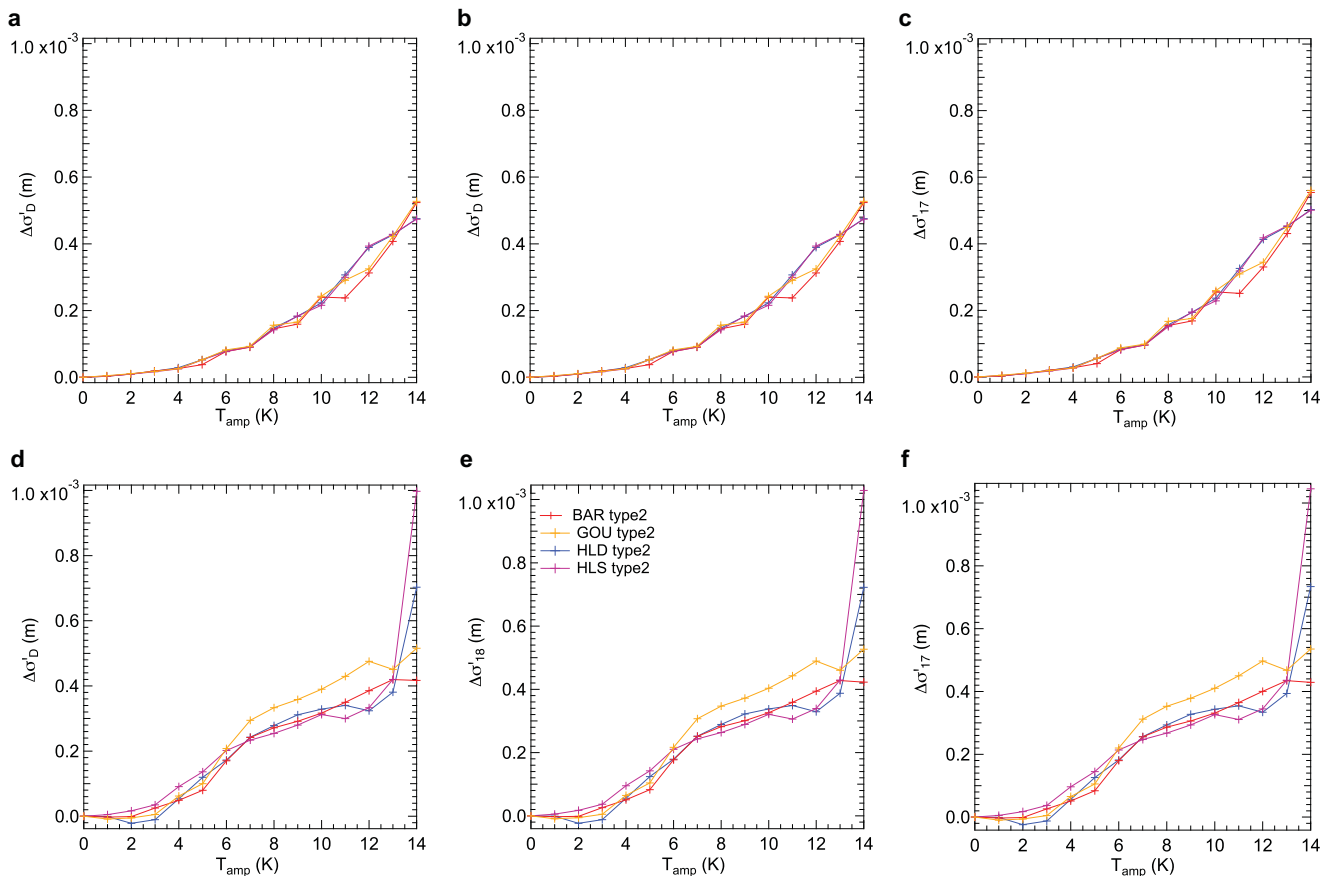


Fig. 9. Seasonal cycle amplitude test for type 1 (subplots a, b, c) and type 2 (subplots d, e, f) conditions. The $\Delta\sigma'$ notation represents the difference $\sigma'(T_{\text{amp}} = T_{\text{amp}}^k) - \sigma'(T_{\text{amp}} = 0)$ with $k \in [0, 14 \text{ K}]$ and T_{amp} the amplitude of the seasonal temperature signal.

It should be mentioned that the densification models tested here, even though typically used for ice core studies may not be the best choices for investigating the influence of the seasonal cycle of temperature. Preliminary results from densification studies using firn compaction data from South Pole and the EastGRIP sites, indicate that the four models tested in this study tend to underestimate the influence of the seasonal signal on the densification process. Further tests including other densification modelling approaches – some of them already present in Iso-CFM – can provide better answers.

Transient simulations

Ramp experiments

We test the performance of the diffusion models for the case of a transient simulation where the climate forcing ramps from low to high temperature–accumulation conditions. The total time of the simulation is 10 000 years and it consists of 4000 years of steady-state conditions with $T = 233.15 \text{ K}$ and $A = 0.1 \text{ m a}^{-1}$ ice eq., a linear climatic transition to $T = 248.15 \text{ K}$ and $A = 0.2 \text{ m a}^{-1}$ ice eq. spanning 2000 years and steady-state conditions thereafter. The heat diffusion module of the model is enabled. The forcing of the experiment is illustrated in Figure 10a. In Figure 10b we present the close-off depth ($\rho_{\text{co}} = 804.3 \text{ kg m}^{-3}$) for all four models at every time step of the simulation and the results for σ'_D , σ'_{18} and σ'_{17} are given in Figure 11. In addition to the four model implementations, the analytical solution using the Herron and Langway steady-state implementation for σ'_{17} , σ'_{18} and σ'_D is evaluated for the climate forcing of the experiment and illustrated as well.

As in the results of Section ‘Steady-state climate forcing’, the first 4000 years of the simulation ($t_{\text{model}} \in [-10\,000, -6000 \text{ years}]$) under steady-state climate, reveal the differences between the densification rate sensitivities of the different models to temperature and accumulation. An interesting aspect of the ramp experiment is the observation of the response time of the models. As the warming signal diffuses into the firn, one should expect a delay at the onset of the temperature and accumulation rise between the forcing and the σ' signals. A difference of ≈ 400 years is observed between the onset of the forcing transition and the first upward change in the value of σ'_{18} . The magnitude of the delay does not vary between the different diffusion length signals (σ'_D , σ'_{18} and σ'_{17}) with the delay itself being slightly shorter than the age of the close-off depth (≈ 500 years – Fig. 10b), pointing to the combined effect of the advection and diffusion acting more effectively in transmitting the warming signal in the firn column. As the climate forcing reaches steady-state conditions at $t_{\text{model}} = -4000$ years the response of the diffusion length signal is delayed by only ≈ 175 years, a number that reflects the shallower close-off depth for the higher temperature–accumulation conditions. A closer look into the firn temperature profile signal reveals a temperature gradient that persists for more than 2000 years after $t_{\text{model}} = -4000$ years. This diminishing temperature gradient results in a very slowly changing value of σ'_{18} through this time interval, which does not settle until the end of the simulation time ($t = 0$). For a visualisation of this effect the reader is referred to the animation `HLdynamic_ramp.mp4` included in the SOM.

Additionally, we present the effects of the temperature and accumulation rate change separately on both the diffusion length and the close-off depth. In Figure 12, the solid lines show the effect of temperature in increasing the diffusion length and

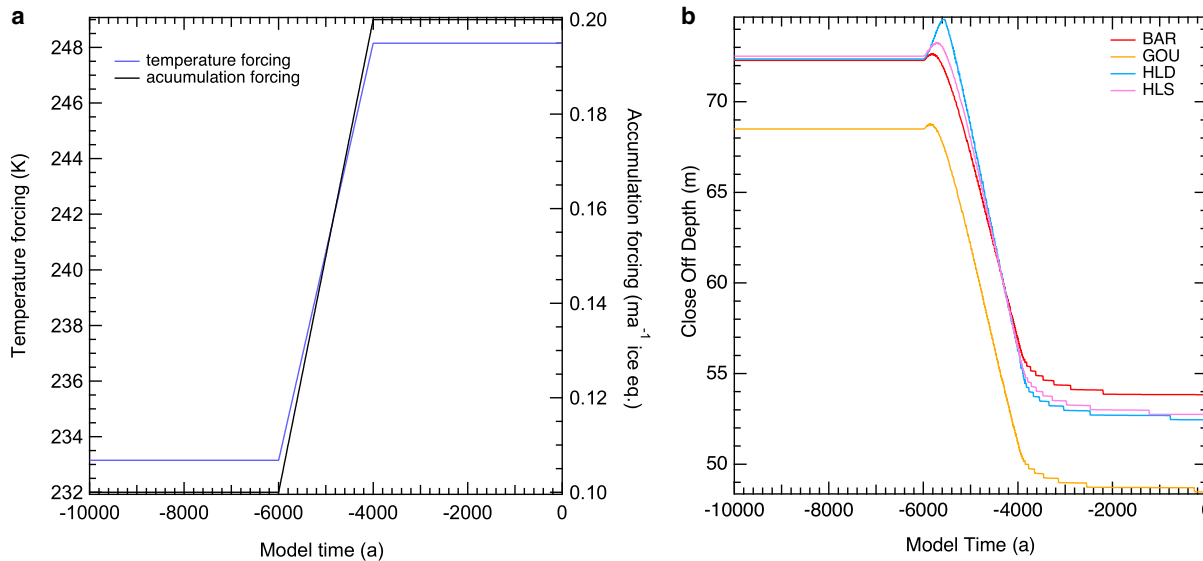


Fig. 10. (a) Temperature and accumulation forcing for the transient simulation. (b) The close-off depth for the transient simulation and the age at the close-off depth modelled with the BAR model.

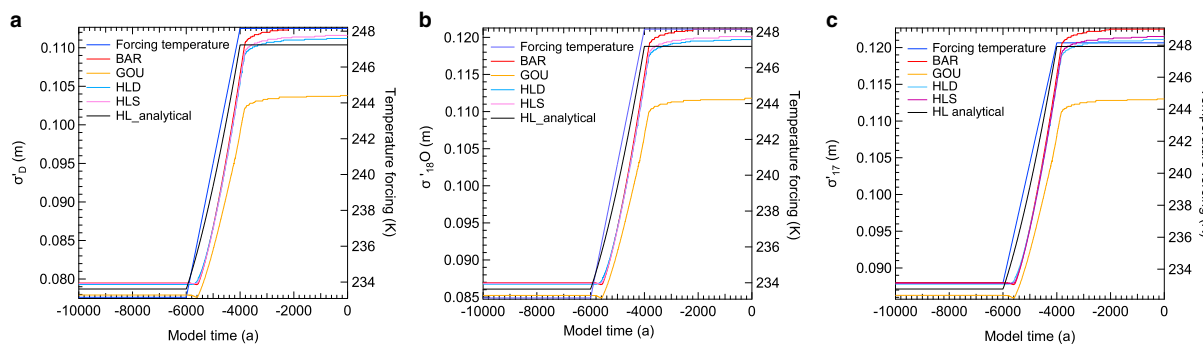


Fig. 11. Transient simulation results for the diffusion length at the close-off depth expressed in m of firn at the close-off density: (a) σ'_D , (b) σ'_{18} , (c) σ'_{17} . The black line represents the diffusion length value as calculated using the steady-state analytical expressions from Eqns (29) and (30).

shallowing the close-off depth as the accumulation is kept constant and the temperature increases. Similarly, the dash lines represent the experiments for which we isolate the impact of the accumulation rate change while the temperature is kept constant. It is apparent that the temperature change of 15 K has a greater impact on the value of the diffusion length compared to that of the doubling of the accumulation rate. We also observe that when the accumulation is doubled while the temperature is kept constant, the differences between the four models are far greater for the close-off values whereas the diffusion length results are comparable for the four model implementations.

Warming pulse experiments

We investigate the models’ response to a warming pulse with a forcing that consists of an initial steady-state period, followed by a rapid warming and cooling phase. The pulse lasts 2000 years, has a temperature magnitude of 10 K (223.15 – 233.15 K) and an accumulation magnitude of 0.05 ma⁻¹ ice eq. (0.05 – 0.1 ma⁻¹). In order to assess the evolution of σ'_{18} under various warming and cooling rates, we introduce a characteristic time ψ that controls the rate of change for the temperature and accumulation forcing signals at the onset and end of the pulse. The forcing signal can be described as (Eqns

33 and 34):

$$\begin{aligned}
 &T_{\text{forcing}} = 233.15 \quad -1000 < t_{\text{model}} \leq 0 \\
 &T_{\text{forcing}} = 233.15 + 10 \left(1 - \exp \left(-\frac{t_{\text{model}} - t_{\text{on}}}{\psi} \right) \right) \\
 &0 < t_{\text{model}} \leq 2000 \\
 &T_{\text{forcing}} = 233.15 + T_{\text{off}} \exp \left(-\frac{t_{\text{model}} - t_{\text{off}}}{\psi} \right) \\
 &2000 < t_{\text{model}} \leq 10\,000
 \end{aligned}
 \tag{33}$$

and

$$\begin{aligned}
 &A_{\text{forcing}} = 0.05 \quad -1000 < t_{\text{model}} \leq 0 \\
 &A_{\text{forcing}} = 0.05 + 0.05 \left(1 - \exp \left(-\frac{t_{\text{model}} - t_{\text{on}}}{\psi} \right) \right) \\
 &0 < t_{\text{model}} \leq 2000 \\
 &A_{\text{forcing}} = 0.05 + A_{\text{off}} \exp \left(-\frac{t_{\text{model}} - t_{\text{off}}}{\psi} \right) \\
 &2000 < t_{\text{model}} \leq 10\,000
 \end{aligned}
 \tag{34}$$

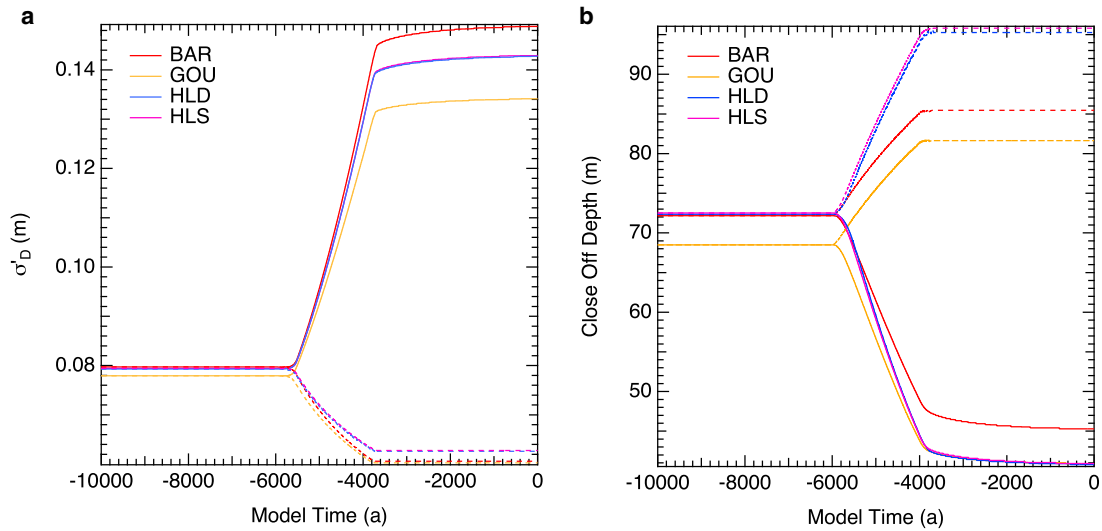


Fig. 12. Individual effect of the temperature and the accumulation forcing on the diffusion length (a) and the close-off depth (b). Solid (dash) lines represent the experiments for which the accumulation (temperature) has been kept constant.

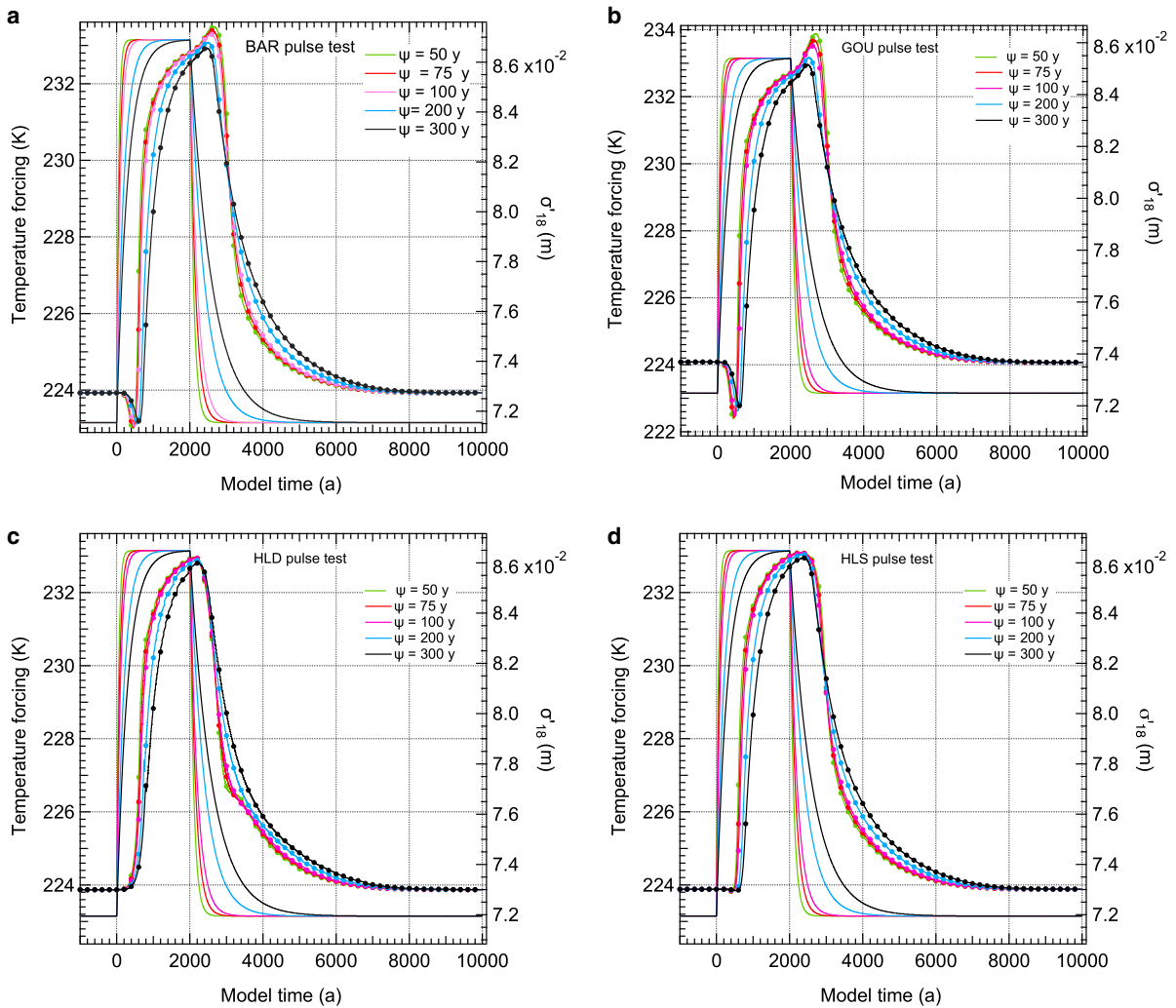


Fig. 13. Results of pulse test for BAR, GOU, HLD and HLS models (subplots a–d), for $\psi = 50, 75, 100, 200, 300$ years. The solid lines represent the temperature forcing while lines with bullet markers represent the diffusion length signal.

We implement five forcing scenarios with $\psi = 50, 75, 100, 200, 300$, years. For all scenarios, $t_{on} = 0$ year, $t_{off} = 2000$ years, and T_{off} and A_{off} are determined by the value of $T_{forcing}$ and $A_{forcing}$ at $t_{model} = 2000$ years. The spin-up run is 4000 years long

($-5000 < t_{model} < -1000$, not shown in Figure 13) and the thickness of the firm column under consideration is 200 m. We use a time step of 1 year, $\rho_0 = 350 \text{ kg m}^{-3}$ and $P = 0.7 \text{ Atm}$. We present the results of the warming pulse experiment in Figures 13a–d, and

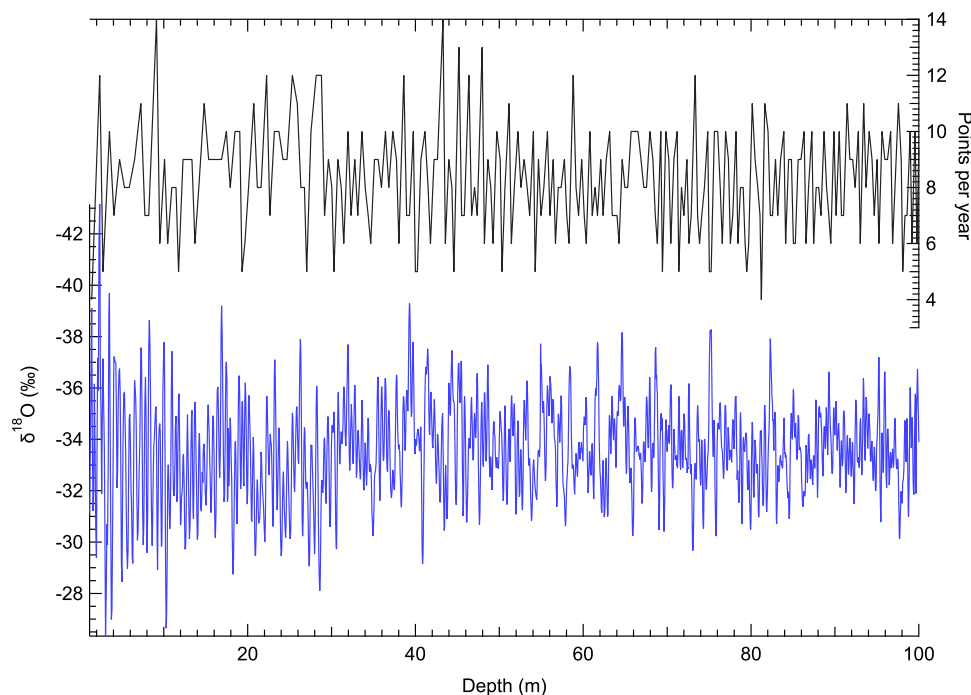


Fig. 14. High-resolution $\delta^{18}\text{O}$ record from the Site-A shallow core. The number of data points per year is given in the top curve.

in the animation `HLdynamic_RC_tau_100.mp4` in the SOM. Based on the outcome of the simulations, the following observations can be made.

For all the simulations there is a time delay between the onsets of the warming signal and the diffusion length signal σ'_{18} . The delay is similar between all the models considered and approximately equal to the age of the close-off depth which for the warm phase climate conditions of the simulation is ≈ 400 years. We also observe that longer characteristic times ψ , result in an increasingly longer delay, reflecting the combined effect of the slower shallowing of the firn column as well as the slower penetration of heat in the firn due to the less steep temperature and accumulation gradients.

The test reveals the differences between the models' dynamic behaviour under changing climate forcing at various rates. Overall, the models show a comparable behaviour across all the rates of change scenarios, although a notable difference can be observed in the initial fast decrease of the diffusion length value at the onset of the warming for the GOU and BAR models, in the order of 10^{-3} m. Similarly, the same models overshoot at the beginning of the cooling phase of the pulse, a behaviour that is followed within 100–200 years by the expected behaviour of a decreasing diffusion length during the cooling phase of the pulse.

This seemingly counter-intuitive result depends on the time constant ψ and is more profound for pulses of higher rapidity (low ψ values). Simulations where we have separated the temperature and accumulation effects on the diffusion length signal show that the BAR and particularly the GOU model result in a more rapid decrease in the σ'_{18} signal when we only change the accumulation and keep the temperature constant. On the other hand, when we introduce pulses of temperature keeping the accumulation constant, the rate of change of the σ'_{18} signal is very similar for all four models (see Figs 20 and 21 in the Appendix) This initial, accumulation-induced, rapid decrease in the σ'_{18} signal overcomes the effect of temperature especially for the GOU model although its duration is short-lived and is followed by an increase in the σ'_{18} signal, concomitant to the temperature increase.

A closer look at the warming phase of the experiment reveals that the σ'_{18} value does not reach steady-state for any of the models and characteristic times considered. Later, as the temperature and the accumulation decreases at $t_{\text{model}} = 2000$ years, the value of σ'_{18} decreases with a long decay time. This decay is due to the residual heat in the firn column, which results in a temperature gradient that persists for ≈ 6000 years. This effect can be of importance for the study of the σ'_{18} signal at millennial time scales and for the purpose of reconstructing past temperatures. The use of an analytical model approach based on the inversion of Eqns (29) and (30) for temperature and assuming steady-state will result in a less accurate temperature estimation over strong and abrupt climatic transitions.

Annual signal attenuation – Site-A

Using the diffusion length calculation, one can estimate the attenuation of the isotopic signal as a function of wavelength for different depths. The transfer function of the diffusion process is equal to

$$\hat{G} = e^{-2(\pi\sigma/\lambda)^2} \quad (35)$$

where λ is the wavelength of the isotopic signal. As a result isotopic cycles with an initial magnitude equal to Γ_0 will be attenuated to (Gkinis and others, 2014; Kahle and others, 2018)

$$\Gamma = \Gamma_0 e^{-2(\pi\sigma/\lambda)^2}. \quad (36)$$

Here, σ is the diffusion length parameter equivalent to the SD of the Gaussian filter in Eqns (2) and (3).

We consider here the shallow core from Site-A, drilled in central Greenland in 1985 (Clausen and Hammer, 1988; Vinther and others, 2010) at 70.63°N, 35.82°W and an elevation of 3092 m. The mean annual temperature at Site-A is -29.4°C and the annual accumulation is 0.29 m ice eq. A high-resolution $\delta^{18}\text{O}$ record exists from this core (Fig. 14). The core was sampled at a variable sampling resolution with the aim of resolving the annual $\delta^{18}\text{O}$ signal. In addition, the sampling resolution is 0.08

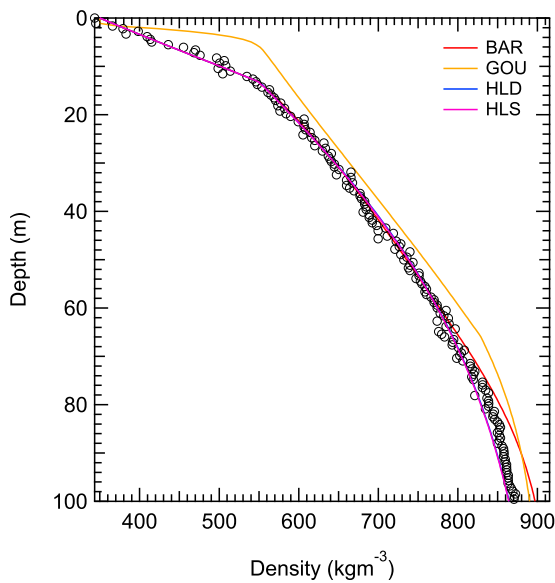


Fig. 15. Measured density profile for the Site-A shallow core and CFM modelled profiles.

m and gradually increases to the value of 0.035 m at the bottom of the core. In Figure 14 we present the number of data points per year as deduced by manually counting the $\delta^{18}\text{O}$ annual cycles from summer to summer. The annual component of the $\delta^{18}\text{O}$ signal survives the effect of diffusion throughout the firn column, a result of the rather special combination of the low temperature and the relatively high accumulation rate. In the study of Clausen and Hammer (1988), $\delta^{18}\text{O}$ is used for the counted chronology of the core. Here, we use the counted chronology in order to infer the annual layer thickness λ_A as a function of depth. We use a third order smoothing spline through the counted chronology-based annual layer thickness (Fig. 16).

Estimating signal attenuation from the $\delta^{18}\text{O}$ record

In order to estimate the annual signal attenuation based on the high-resolution $\delta^{18}\text{O}$ record, we make use of the analytical integration technique for spectral peaks described in Johnsen and Andersen (1978). We calculate the power spectral density of 5

m sections of the $\delta^{18}\text{O}$ signal using the maximum entropy method (MEM hereafter) (Burg, 1975). For every 5 m section we interpolate the $\delta^{18}\text{O}$ time series on the mean resolution of the section. Subsequently, using the autoregressive coefficients of the MEM prediction filter, we perform an analytical calculation of the position (in the frequency space) and the total area of the annual spectral peak. This in turn yields an estimate of the annual layer thickness λ_A (in other words the wavelength of the $\delta^{18}\text{O}$ annual signal) and the mean magnitude of the annual component (hereafter Γ_A) in the $\delta^{18}\text{O}$ signal for every 5 m depth interval. The value of Γ_A for the top depth interval is equal to $\Gamma_{A0} = 2.5\text{‰}$ and is used to obtain a data-based estimate of the signal attenuation as a function of depth.

We perform a steady-state 1000 years run in the Iso-CFM for every of the four model implementations considered here. Estimates of the density profiles are compared to the measured densities from the site (Fig. 15). The comparison reveals a profound mismatch between the GOU model and the measured density profile, with the model predicting faster densification rates throughout the full firn column. The HLD and HLS implementations show the best agreement whereas the BAR model deviates from the data for densities above 800 kg m^{-3} . Using the modelled σ_{18} signal we calculate the decay of the magnitude of the annual signal $\Gamma_A/\Gamma_{A0} = \exp(-2\pi^2\sigma_{18}^2/\lambda_A^2)$ where λ_A is the spline-smoothed annual layer thickness based on the counted chronology.

The results of the model and data-based spectral estimation of the annual signal magnitude decay are shown in Figure 16. We see that the HLD and HLS type models are the most accurate in predicting the attenuation of the annual signal. The observed and modelled annual signal magnitudes, decay exponentially with depth until the close-off depth after which they reach a constant value. The faster densification rates predicted by the GOU model yield a lower value for the diffusion length σ_{18} . As a result the GOU-inferred magnitude of the annual signal is higher than all the other models as well as the data-based magnitude. The slight discrepancy between the BAR model and the measured density at the bottom of the core results in a mismatch between the BAR-modelled and the data-based annual signal magnitude. This result shows how the densification of firn can have an effect on the diffusion length signal even past the close-off depth ($\approx 70.9 \text{ m}$) and thus in parts of the firn where the diffusion process has ceased.

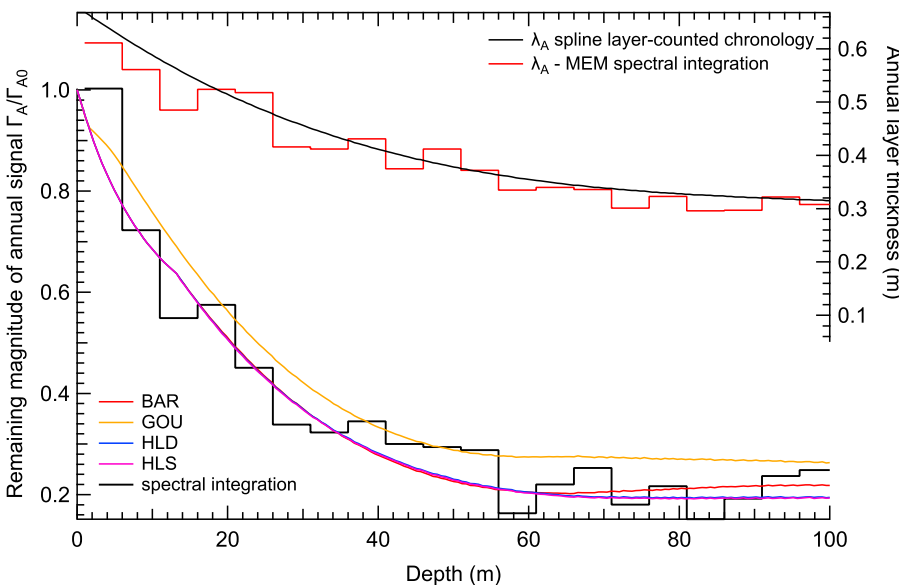


Fig. 16. Annual signal magnitude decay and annual layer thickness λ_A for the Site-A shallow core. We estimate independently the annual layer thickness λ_A from (1) the counted annual layers fitted with a smoothing spline and (2) by means of the spectral peak detection/integration technique in the MEM power spectrum (Johnsen and Andersen, 1978) at 5 m resolution sections. The black solid line in the bottom plot represents the magnitude of the annual signal as estimated using the spectral peak analytical integration method whereas the coloured lines are calculated using the Iso-CFM σ_{18} profiles in combination with spline smoothed annual layer thickness λ_A profile based on the counted chronology.

Table 2. Ice core data sections and the corresponding drill site characteristics

Site	Depth m	Age ka b2k	Present T K	A m ice a^{-1}	P Atm	Thinning	Surface density ρ_0 kg m^{-3}
Dome F ^a	302–307	9.6	215.8	0.03	0.61	0.93	330
Dome C ^b	308–318	9.9	219.7	0.03	0.65	0.93	330
EDML ^c	140–150	1.6	228.6	0.07	0.67	0.93	330

A summary of the datasets can also be found in Holme and others (2018).

Source of data: Svensson and others (2015)^a, Gkinis (2011)^b, Oerter and others (2004)^c.

Data-based temperature estimates

We present here a test of the temperature reconstruction method using ice core diffusion length data from the study of Holme and others (2018).

Description of the ice core datasets

The ice core sites considered are Dome F, the Dome C and the EDML. For site characteristics and data references see Table 2. All the sections considered here contain data from depths below the close-off, though still relatively shallow compared to the full length of the cores. This has a threefold advantage: (a) the effect of solid ice diffusion is negligible, (b) the ice flow thinning is minimal and accurately constrained and (c) the accumulation rate for all three sites shows very small deviations compared to present for the time windows considered (Veres and others, 2013).

The three datasets have each been measured with a different analytical technique. For the EDML and Dome C sections, two different Isotope Ratio Mass Spectrometry techniques were used (Oerter and others, 2004; Gkinis, 2011). The Dome F section has been analysed with Cavity Ring Down Spectrometry using a continuous flow analysis approach (Gkinis and others, 2011; Svensson and others, 2015). For all sections, $\delta^{18}O$ and δD data are available, thus allowing for a comparison between the reconstructions of the two diffusion length signals. Moreover, two published temperature reconstruction studies (Stenni and others, 2010; Uemura and others, 2012) based on the isotope mixed cloud model (hereafter IMCM) (Ciais and Jouzel, 1994) are available, allowing for a comparison of our results with the more traditional water isotope thermometer method using the combined δD , D_{excess} signal to infer site–source temperature variations.

The two East Antarctic sites included in this test (Dome F and Dome C) are particularly interesting as they are characterised by a very similar annual accumulation signal while there is a difference of ~ 4 K in the present temperature signal. A strong accumulation intermittency is also observable with only a few events comprising the total annual accumulation. Although the prevalent conditions at the site are cold and dry, with typical occurrence of clear sky precipitation, a significant part of the snowfall takes place under rare episodes of warmer conditions (Fujita and Abe, 2006). These features can possibly pose a challenge to the classical isotope palaeothermometer (Fujita and Abe, 2006; Schlosser and others, 2017) by introducing biases due to (a) the non-representative temperatures under which precipitation is formed (b) the occurrence of kinetic effects observed under such cold and dry conditions. On the other hand, the diffusion process that we consider here is not affected by such effects, as the diffusion length for a certain temperature is independent of the initial isotopic signal at the surface. Although the traditional isotopic thermometer ‘samples’ individual precipitation events, diffusion is continuously affected by the temperature and the accumulation signal at the surface and the firn column.

Methodology and results of the experiment

The diffusion length estimates used for the three sections considered are presented in Table 4 of Holme and others (2018). These values are given in m of ice equivalent and have been corrected for the effects of ice diffusion and sampling mixing as well as for the ice flow thinning. For a detailed description on the diffusion length estimation from high-resolution isotope data and the necessary corrections involved, the reader is referred to the methods sections in Gkinis and others (2014) and Holme and others (2018).

We convert the ice equivalent diffusion length values from Table 4 in Holme and others (2018) to m of firn equivalent at the depth of the close-off density $\rho_{\text{co}} = 804.3 \text{ kg m}^{-3}$ by scaling with the factor $\rho_{\text{ice}}/\rho_{\text{co}}$. This scaling yields the data-based estimate of the diffusion length $\hat{\sigma}'$. Subsequently, we estimate the root of the equation $\sigma'(T, \rho = \rho_{\text{co}}) - \hat{\sigma}' = 0$ from which an absolute temperature estimate in K is obtained. For the root finding step we use Brent's algorithm (Brent, 1973; Press and others, 2007) and require a tolerance for the estimated root equal to 0.01 K. Every calculation of $\sigma'(T, \rho = \rho_{\text{co}})$ is based on a 2500 years run of the model. We use the uncertainties of the diffusion length estimation from Table 4 in Holme and others (2018) and generate normal distributions for the value of $\hat{\sigma}'$, which in turn yield a distribution of temperatures for each ice core site. The size of the distributions is equal to 500. For all our calculations the fractionation factors from Majoube (1971) and Merlivat and Nief (1967) are used.

The mean and SDs of $\hat{\sigma}'$ and the estimated temperatures for all sites and all models are shown in Tables 3 and 4 and their relative distributions are presented in Figure 17. Overall, the results of the experiment indicate that the combined uncertainty of the four models is in the order of 0.5 K for all sites considered. The two isotopes yield very similar results (within 1-SD) for the Dome C and EDML sites, whereas the Dome F reconstruction indicates a slightly larger discrepancy between the $\hat{\sigma}'_D$ and the $\hat{\sigma}'_{18}$ based temperature estimates (marginally over 2-SDs).

In Table 5 we present the comparison of our results with the present temperature as well as the temperature estimates for the time windows under consideration based on the IMCM. The youngest age of the Dome F and Dome C temperature reconstructions is 100 years B.P. (Stenni and others, 2010; Uemura and others, 2012) and is used as equivalent to present conditions for our comparison. The EDML reconstruction on the other hand has a youngest age of 1300 years B.P. (Stenni and others, 2010), so in order to compare to present, we use the regional reconstruction from PAGES 2k Consortium (2013) and account for a mean temperature anomaly of 0.43 K between present and the reference period 1.2–2 ka B.P. in Stenni and others (2010). The comparison is presented in Figure 17 where the dot and dot-dash vertical lines represent the diffusion and the IMCM temperature estimates respectively. The two techniques agree within 1-SD (we refer to the SD of the diffusion reconstruction). The IMCM estimates do not have an adjoint uncertainty interval) for the Dome F and Dome C sites. On the other hand, the EDML reconstructions differ by 1.1 K, a result that lies outside of the 3-SD interval of the diffusion estimate and which we comment

Table 3. Results of the ice core data experiments for $\delta D - \hat{\sigma}_D$

Site	Present T K	$\hat{\sigma}'_D$ (Holme and others, 2018) cm	T_{D-BAR} K	T_{D-HLD} K	T_{D-HLS} K	T_{D-GOU} K	T_{D-all} K
Dome F	215.8	5.61 ± 0.07	214.6 ± 0.2	214.8 ± 0.3	214.8 ± 0.3	214.1 ± 0.2	214.6 ± 0.4
Dome C	219.7	7.23 ± 0.09	220.5 ± 0.2	221.1 ± 0.3	221.1 ± 0.3	220.7 ± 0.3	220.9 ± 0.4
EDML	228.6	8.11 ± 0.09	229.3 ± 0.3	229.8 ± 0.3	229.8 ± 0.3	229.9 ± 0.3	229.7 ± 0.4

Table 4. Results of the ice core data experiments for $\delta^{18}O - \hat{\sigma}_{18}$

Site	Present T K	$\hat{\sigma}'_{18}$ (Holme and others, 2018) cm	T_{18-BAR} K	T_{18-HLD} K	T_{18-HLS} K	T_{18-GOU} K	T_{18-all} K
Dome F	215.8	6.56 ± 0.17	215.5 ± 0.5	215.7 ± 0.6	215.7 ± 0.5	214.9 ± 0.5	215.5 ± 0.6
Dome C	219.7	7.94 ± 0.16	220.3 ± 0.4	220.9 ± 0.5	220.9 ± 0.5	220.4 ± 0.5	220.6 ± 0.5
EDML	228.6	8.80 ± 0.09	229.0 ± 0.3	229.5 ± 0.3	229.5 ± 0.3	229.6 ± 0.3	229.4 ± 0.4

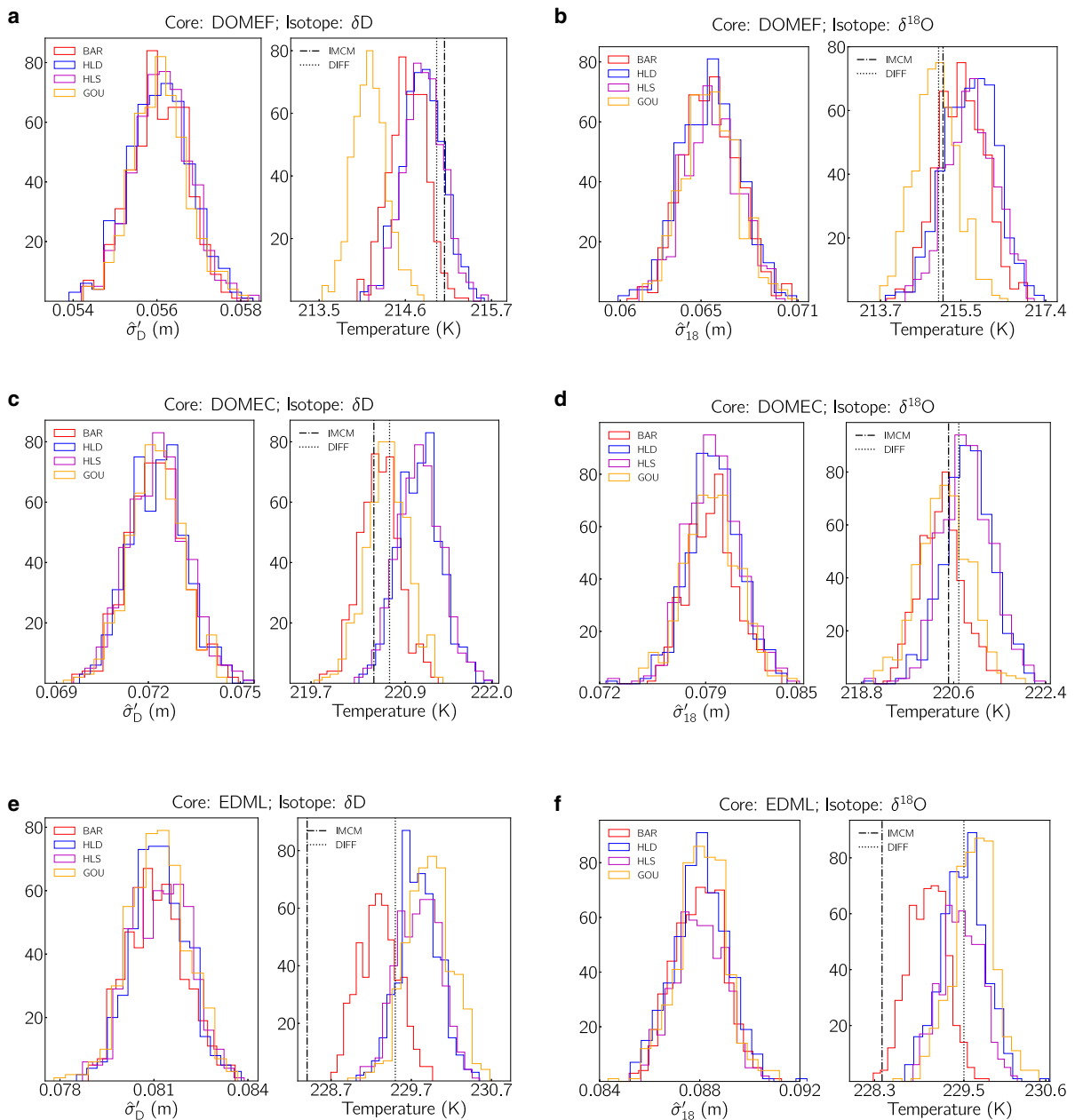


Fig. 17. Results of the temperature estimation test for three Antarctic sites. For every core and every isotopologue we present the starting distribution for the diffusion length signal as found in Holme and others (2018) and scaled to its close-off density value $\hat{\sigma}'_{18}$ (m of firm eq.) as well as the resulting temperature distributions for all four models. Dot-dash lines represent the temperature estimate based on the IMCM and dot lines represent the mean temperature estimate based on both the $\hat{\sigma}'_D$ and the $\hat{\sigma}'_{18}$ reconstructions.

Table 5. Comparison between the diffusion and the IMCM temperature reconstructions

Site	Present T K	T_{IMCM} K	$T_{18\text{-all}}$ K	$T_{\text{D-all}}$ K	$T_{\text{diffusion-all}}$ K
Dome F	215.8	215.1 ^a	215.5 ± 0.6	214.6 ± 0.4	215 ± 0.6
Dome C	219.7	220.5 ^b	220.6 ± 0.5	220.9 ± 0.4	220.7 ± 0.3
EDML	228.6	228.4 ^{b,c}	229.4 ± 0.4	229.7 ± 0.4	229.6 ± 0.3

For Dome F the IMCM temperature reconstruction is from Uemura and others (2012)^a, for Dome C we have used Stenni and others (2010)^b and for EDML we combined the reconstruction from Stenni and others (2010)^b and the PAGES 2k regional reconstruction (PAGES 2k Consortium, 2013). The column $T_{\text{diffusion-all}}$ contains the combined $T_{\text{D-all}}$, $T_{18\text{-all}}$ diffusion-based temperature estimates.

further on, in Section ‘Antarctic sites temperature reconstruction – comparison with the isotope mixed cloud model’.

Diffusion length histories over millennial time scales – the WAIS-D example

We demonstrate here the calculation of diffusion length histories over millennial time scales using the WAIS-D (79.5° S, 112.1° W) ice core as an example. As climate forcing, we use the temperature reconstruction from Cuffey and others (2016) and the accumulation reconstruction from Fudge and others (2016), both smoothed with a 2-order low-pass Butterworth digital filter using a critical period of 10^3 years. Heat diffusion is enabled for all runs. We run two simulations, one with annual resolution and one with monthly resolution with an annual temperature amplitude of 10 K. The simulations are initiated with a 5000 years spin-up run. Based on measured firn density profiles from WAIS-D, we use $\rho_0 = 420 \text{ kg m}^{-3}$.

The simulation shows sizeable signals throughout the whole WAIS-D record due to the combined fluctuations in temperature and accumulation (Fig. 18). The glacial–interglacial transition spanning $\sim 10\,000$ years yields a σ'_{18} signal increase of almost 2 cm, while the increase in the accumulation forcing during the period $-10\,000$ to -2000 years yields a σ'_{18} signal of < 1 cm. The discrepancies between the models are of the order of almost 1 cm and we observe that the GOU and BAR models predict higher

values for σ'_{18} when compared to HLD and HLS. This is not in agreement with the results of the previous sections and in particular Section ‘Steady-state climate forcing’ where similar temperature and accumulation conditions result in the GOU model yielding σ'_{18} values that are lower than those calculated with the HLD and HLS models.

This is due to the different response of the models to changes in the surface density ρ_0 . A higher surface density value results in an overall denser firn column with a lower open porosity available for diffusive mixing. Second, initiating the densification process at a higher density results in an overall shallower firn column with lower values for both the close-off depth as well as the close-off age. As a result, the increase of the surface density shortens the time available for diffusive mixing thus reducing the diffusion length value.

Model runs implementing $\rho_0 = 420 \text{ kg m}^{-3}$ and $\rho_0 = 350 \text{ kg m}^{-3}$ (Fig. 19) indicate that the GOU model shows a minimal response to the change of the surface density. HLD and HLS react stronger to the changes in surface density with a difference of ~ 0.5 cm in terms of σ'_{18} signal, while the BAR implementation lies in between. In the animation file `wais_GOUvsHLS.mp4` in the SOM, we focus on the comparison between the GOU and HLS models for the two surface density scenarios. The animation allows for an inspection of the density and diffusion length vertical profiles for every time step of the model runs. A comparison between the GOU runs for $\rho_0 = 350 \text{ kg m}^{-3}$ and $\rho_0 = 420 \text{ kg m}^{-3}$ reveals that the density profiles differ only from the surface and until the depth of the critical density which for the case of the GOU model is 600 kg m^{-3} . The higher surface density scenario ($\rho_0 = 420 \text{ kg m}^{-3}$) densifies slower in this upper stage of densification. Below the critical density depth, the two profiles are identical thus the diffusion length profiles and eventually the σ'_{18} values show marginal differences. On the contrary, the HLS model presents a consistent difference between the two density profiles with the $\rho_0 = 420 \text{ kg m}^{-3}$ profile being denser from the surface and until the firn–ice transition where the two profiles progressively converge.

Changes in the climate forcing can result in changes in the surface density over centennial and especially millennial scales. Based

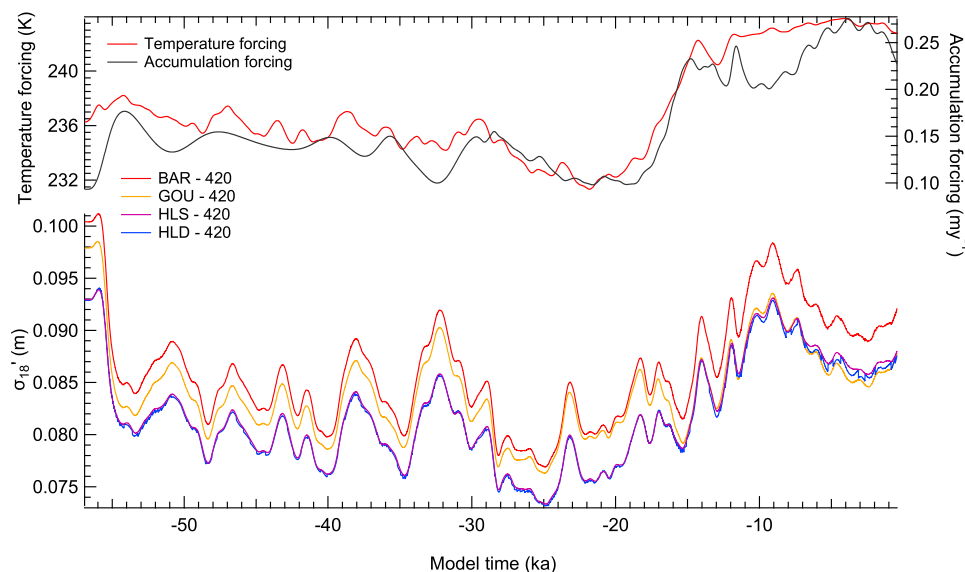


Fig. 18. WAIS-D diffusion length history for $\delta^{18}\text{O}$. With σ'_{18} we symbolise the value of the diffusion length at the close-off depth ($\rho_{\text{co}} = 804.3 \text{ kg m}^{-3}$) in m of firn equivalent. The BAR, GOU, HLD and HLS model implementations are used with and without a seasonal cycle in temperature (runs with seasonality are visually indistinguishable from those without, therefore they are removed from the figure for clarity). The temperature and accumulation forcing signals (top subplot) are smoothed with a 1000-year low pass Butterworth filter. All simulations use a surface density $\rho_0 = 420 \text{ kg m}^{-3}$.

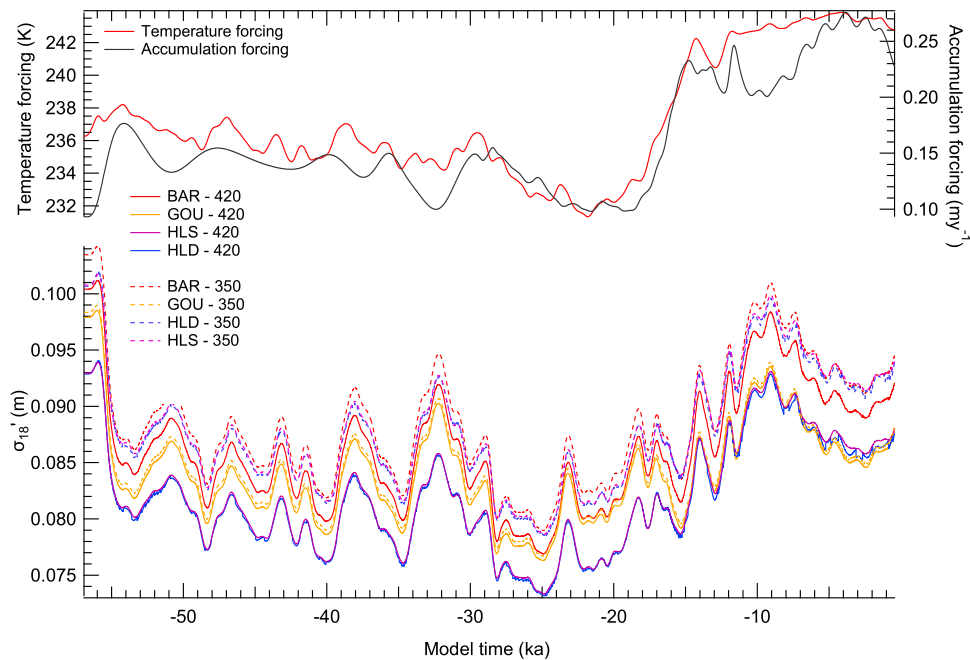


Fig. 19. WAIS-D diffusion length history for $\delta^{18}\text{O}$. With σ'_{18} we symbolise the value of the diffusion length at the close-off depth ($\rho_{co} = 804.3 \text{ kg m}^{-3}$) in m of firm equivalent. The BAR, GOU, HLD and HLS model implementations are used and a comparison between two model arrangements using different surface densities ($\rho_0 = 350 \text{ kg m}^{-3}$ – dash lines and $\rho_0 = 420 \text{ kg m}^{-3}$ – solid lines). The temperature and accumulation forcing signals (top subplot) are smoothed with a 1000-year low-pass Butterworth filter.

on the study from Kaspers and others (2004) the surface density can be linked to temperature T (K), accumulation A (m a^{-1} ice eq.) and wind velocity W (m s^{-1}) using the empirical form:

$$\rho_0 = 7.36 \times 10^{-2} + 1.06 \times 10^{-3}T + 6.69 \times 10^{-2}A + 4.77 \times 10^{-3}W. \quad (37)$$

The coefficients in Eqn (37) are estimated using present day data from 40 individual measurements from various Antarctic sites. Based on the present T and A conditions at WAIS-D and a surface density of $\rho_0 = 420 \text{ kg m}^{-3}$ we deduce $W = 16 \text{ m s}^{-1}$. Extrapolating Eqn (37) in time and assuming the same wind conditions, a reduction of temperature by 15 K and of accumulation by 50% would yield a surface density of $\rho_0 = 400 \text{ kg m}^{-3}$. Although still a sizeable change, it is not expected to affect our calculations significantly. The implementation of Eqn (37) in the Iso-CFM can be a further step to include the dependence of the surface density on the climate conditions of the site considered.

Including temperature seasonality in our calculations for WAIS-D does not have any significant effect for any of the densification models used (Fig. 18). It is worth mentioning that the increase of time resolution from annual to monthly iterations imposes a twofold burden on the computational load. The first, which is expected to be roughly linear, relates to the increase in the total number of model iterations. The second concerns the total number of grid points in the depth domain, which increases proportionally with the number of time steps per model-year. The matrix operations occurring in the Iso-CFM, particularly those involved in the calculations of the heat diffusion can be heavily affected by a significant increase in the number of grid points. Therefore, performance tests where these parameters are assessed are recommended depending on the application.

Discussion

The behaviour of the four models under steady-state and dynamic conditions

Our results indicate that there are differences between the four different densification models, both with respect to the steady state as well as the dynamic behaviour. For the first case, we see that differences in the densification rates under steady-state conditions result in discrepancies in the diffusion length profiles and consequently in the values of the diffusion lengths at close-off. We find that despite the fact that all four models follow an Arrhenius formulation for the activation energy, the GOU model tends to densify faster in the higher temperature–higher accumulation range. This result is isotope independent and therefore the discrepancies are apparent for all three isotopes (σ'_D , σ'_{18} , σ'_{17}). Tests on the dynamic behaviour of the models show that the GOU model is more sensitive to accumulation changes resulting in a denser upper firm faster and as a consequence in a more rapid decrease of the σ'_{18} signal. We find that this discrepancy depends on the rapidity of the accumulation rate change with more rapid changes resulting to poorer agreement between the models – in particular the GOU model. On the other hand, the dynamic response of all four models to temperature-only changes is much more similar, owing most likely to the Arrhenius type temperature dependence.

Results from Site-A and the temperature regime above 235 K

Based on the data-model comparison for Greenland Site-A in section 'Annual signal attenuation – Site-A', we see that the HLD and HLS models are the most adequate in describing the densification and the isotopic signal attenuation processes. The GOU model predicts densification rates that are higher than what the data indicate and as a result yields lower diffusion rates. The origin of this result can be traced back to the temperature sensitivity of the GOU model that yields lower diffusion length values

compared to the other three models for temperatures higher than 235 K, (Fig. 5). This result suggests that the GOU model should be used with caution for site temperatures above 235 K, a range that corresponds to typical conditions for many Greenland ice core sites.

Antarctic sites temperature reconstruction – comparison with the IMCM

When considering the temperature reconstructions for the Antarctic sites in section ‘Data-based temperature estimates’, we observe a good agreement between all four models especially for the cases of Dome C and EDML sites. These two sites lie in a temperature range where the temperature sensitivities of the densification models do not show any noticeable differences (Fig. 5). For the colder Dome F site, the GOU model predicts higher diffusion rates (Fig. 5) and as a result the model infers a colder temperature. The comparison of the diffusion-derived temperature reconstructions to published temperature estimates using the traditional IMCM reveals a good agreement between the two methods for the Dome F and Dome C sites. The discrepancy between the two estimates is in the order of 0.2 K, which is within 1-SD of the diffusion-based estimate. On the other hand, the comparison of the two techniques for the EDML site reveals a larger discrepancy that lies out of the 3-SD interval and is equal to 1.1 K. Part of this discrepancy could be due to the fact that for this comparison we have used the generic, regional Antarctic temperature anomaly estimate from PAGES 2k Consortium (2013) in order to extend the IMCM reconstruction by Stenni and others (2010) to present conditions. Additionally, a proper comparison between the two techniques should take into account the uncertainty intervals of both methods, however none of the IMCM temperature reconstructions for the sites considered here comes with an uncertainty estimate. One important aspect of the diffusion-based temperature reconstruction method is that it yields absolute temperatures. Therefore, tuning of the model to the present isotopic composition of the precipitation, a step necessary for the IMCM, is not a requirement for the diffusion thermometer. Absolute temperature estimates also have the advantage that they do not depend on a reference period. It is typical for IMCM reconstruction to report temperature deviations from the mean level of a period that can be as long as 2000 years (as is the case for Dome F), a complexity that is not apparent in the case of the diffusion-based temperature reconstruction.

The influence of the seasonal cycle

An interesting result of our calculations is that the influence of the temperature seasonal cycle on the diffusion length calculation is minimal. This result applies to both of the steady-state climate regimes (low temperature/low accumulation, high temperature/high accumulation) as well as to the calculation of the WAIS-D diffusion length history. This conclusion has some significance for the computational load of modelling runs. For cases where the study of the seasonal cycle is not the primary focus, disabling seasonality can present important improvements in performance without compromising the results of the computation. This result also contradicts previously published results by Simonsen and others (2011). In that study, which used a steady-state analytical diffusion model, the annual temperature signal resulted in slightly higher diffusion length values. A main difference between the two studies is that the amplitude of the annual signal in Simonsen and others (2011) is very high and the temperature reaches values up to 263 K where the non-linearity of the saturation pressure over ice results in excessively high values for the firn diffusivity. For the WAIS-D run with temperature seasonality enabled, the

differences in the diffusion length value were in the order of 10^{-3} cm, practically negligible for the purpose of temperature reconstructions. It is worth noting that the simulations with the seasonality enabled required ~ 10 – 15 times more computing time. As mentioned earlier, the densification models considered in this study may not be the best choices if the seasonal cycle and its influence is the main focus. Further modelling efforts considering densification models tailored for this type of studies and currently available in Iso-CFM (Li and others, 2002; Ligtenberg and others, 2011) can be very useful in the future.

Conclusions – outlook

We have developed a firn-diffusion model for water isotopes and coupled it to the CFM. The model utilises the diffusivity parameterisation by Johnsen and others (2000) with various options for the calculation of the fractionation factor, the saturation vapour pressure and the firn tortuosity and it calculates diffusion length profiles for the three isotope ratios $\delta^{17}\text{O}$, $\delta^{18}\text{O}$, δD . The main inputs of the model are temperature and accumulation, whereas parameters related to the densification and diffusion processes can be altered from the model’s configuration file. The model offers the possibility to model the temperature of the firn column, which is also used for the isotope diffusion calculations. An important note about the model is that it does not require any information about the isotopic signal of the precipitation. The mean level as well as the variability of the $\delta^{18}\text{O}$ signal are irrelevant to the calculation of the diffusion length. As a result, our computational scheme is also not affected by effects that can bias the $\delta^{18}\text{O}$ signal due to for example kinetic effects, atmospheric inversions, or the intermittency of the precipitation.

We have tested the model using four densification models, commonly used in ice core studies; two variations (HLD and HLS) of the Herron and Langway model (Herron and Langway, 1980), the Barnola and Pimienta model (Barnola and others, 1991) (BAR) and the Goujon model (Goujon and others, 2003) (GOU). We described the numerical scheme used for the calculation of the diffusion length and we included the analytical solutions for the case of steady-state conditions that have previously been used in other studies but not presented. Model runs with two types of transient forcing shapes (ramp and pulse) showed that the response of the diffusion length signal at the close-off depth presents a time lag that is roughly equal to the age of the close-off depth for each model, a feature that is common for all four models. An interesting aspect of these results is that models with very similar behaviour for steady-state conditions, can behave differently for dynamic climate forcing scenarios. A seasonal temperature cycle with a constant amplitude has been included in some of the simulations. Enabling this feature in the model can increase the computation load considerably, both with respect to time as well as computing resources. For most of the simulations we ran, the result with the seasonal signal enabled differed marginally from the results of the simulations where the seasonal signal was not enabled. Despite this minimal influence we conclude that for increasingly high seasonality amplitudes (>10 K) the annual temperature cycle can be a parameter that needs to be considered.

A model-data comparison for Site-A, Greenland indicates that the HLD and HLS models are the best in describing both the densification and the diffusion processes whereas the GOU model shows a bias towards faster densification rates and slower diffusion due to its higher temperature sensitivity for temperatures above ≈ 235 K. Based on this result we concluded that the GOU model may be inadequate for the study of ice core sites with these temperature characteristics.

We also demonstrated a simple method for the inversion of the model and for the purpose of temperature reconstructions. We focused on three Holocene high-resolution sections from the Dome F, Dome C and EDML ice core sites already presented in the study Holme and others (2018). Using the data-based diffusion lengths as estimated in Holme and others (2018) and the present day accumulation rates we inverted the model and calculated the temperature for each site. Results indicate a combined uncertainty (considering all four models) of ≈ 0.5 K. A comparison with published temperature reconstructions using the traditional $\delta D - D_{\text{excess}}$ IMCM model (Ciais and Jouzel, 1994) reveals a good agreement between the two techniques with a difference of 0.1, 0.2 and 1.1 K for Dome F, Dome C and EDML sites respectively. A notable advantage of the diffusion-based method is the fact that it yields absolute temperatures instead of anomalies from a reference period as is the case for the IMCM.

Finally, we have demonstrated the use of the model for the calculation of diffusion length histories for deep ice cores. Using the WAIS-D ice core site we showed how the combined changes in temperature and accumulation result in diffusion length signals with an amplitude of ≈ 1 –1.5 cm. Such calculations can be used in an inverse way in order to infer temperature or accumulation histories. The relatively recent advances in measurement techniques have over the last few years made it possible to obtain high-resolution $\delta^{17}\text{O}$, $\delta^{18}\text{O}$ and δD profiles from ice cores in much shorter analysis times with very high precision and accuracy. These datasets can provide accurate estimates of the diffusion length signal as described in previous studies (Gkinis and others, 2014; Jones and others, 2017a; Holme and others, 2018). A combination of these datasets with the Iso-CFM can yield a powerful computation scheme for temperature and accumulation reconstructions based on Monte-Carlo and/or Bayesian inversion techniques. The very characteristics of such reconstructions are dependent on the quality of the data, the site under consideration and the desired accuracy and resolution of the reconstructed signal.

Future efforts using diffusion length signals for the purpose of temperature reconstructions will have to take into account other sources of possible uncertainty that are mainly related to the estimation of the σ'_{18} signal itself (Gkinis and others, 2014; Holme and others, 2018; Kahle and others, 2018). Estimates of the σ'_{18} signal require isotopic datasets at sufficiently high resolution, typically in the order of 10 cm or higher. The required resolution is site-specific and it also depends on the depth interval under consideration. Additionally, measurements with sufficiently high signal to noise ratio are pivotal for this application as they allow for a more robust spectral estimation for σ'_{18} . On the other hand, measurement accuracy is not an important parameter for this application as the mean level of the time series under consideration is always subtracted prior to the spectral estimation step. Additional corrections related to the ice flow thinning and ice diffusion need to be applied. These are also site specific and are currently not included in Iso-CFM. Ice core sections from higher depths will be more prone to uncertainties related to ice flow and in the same time will be more affected by the ice diffusion processes that are progressively stronger as one approaches the bedrock.

Supplementary material. The supplementary material for this article can be found at <https://doi.org/10.1017/jog.2021.1>.

Data. The code for Iso-CFM can be downloaded at https://github.com/vgkinis/iso_cfm.git.

Acknowledgements. We acknowledge funding from the European Research Council under the European Community's Seventh Framework Programme (FP7/2007-2013)/ERC grant agreement No. 610055 (Ice2Ice project) and the Villum Foundation under the Villum Experiment programme (Project No.

00022995). Support for development of the CFM was provided by National Science Foundation Partnerships in International Research and Education (PIRE) grant 0968391. We thank A. Bourantas, T. Laepple, T. Münch and E. Waddington for insightful discussions.

References

- Barkan E and Luz B** (2005) High precision measurements of $^{17}\text{O}/^{16}\text{O}$ and $^{18}\text{O}/^{16}\text{O}$ ratios in H_2O . *Rapid Communications in Mass Spectrometry* **19** (24), 3737–3742. doi: [10.1002/rcm.2250](https://doi.org/10.1002/rcm.2250).
- Barnola JM, Pimienta P, Raynaud D and Korotkevich YS** (1991) CO_2 -climate relationship as deduced from the Vostok ice core: a re-examination based on new measurements and on a re-evaluation of the air dating. *Tellus B* **43**(2), 83–90, ISSN 0280-6509. doi: [10.1034/j.1600-0889.1991.t01-1-00002.x](https://doi.org/10.1034/j.1600-0889.1991.t01-1-00002.x).
- Brent RP** (1973) *Algorithms for Minimization without Derivatives*. Englewood Cliffs, N.J.: Prentice-Hall.
- Buizert C and 13 others** (2014) Greenland temperature response to climate forcing during the last deglaciation. *Science (New York, N.Y.)* **345**(6201), 1177–1180. doi: [10.1126/science.1254961](https://doi.org/10.1126/science.1254961).
- Buizert C, Elias SA and Mock CJ** (2013) *Ice Core Methods – Studies of Firm Air*. Amsterdam: Elsevier, 361–372.
- Burg JP** (1975) *Maximum Entropy Spectral Analysis* (Ph.D. thesis). Stanford University.
- Ciais P and Jouzel J** (1994) Deuterium and oxygen-18 in precipitation: isotopic model, including mixed cloud processes. *JGR: Atmospheres* **99**(D8), 16793–16803.
- Clausen HB and Hammer CU** (1988) The Laki and Tambora eruptions as revealed in Greenland ice cores from 11 locations. *Annals of Glaciology* **10**, 16–22. doi: [10.3189/s0260305500004092](https://doi.org/10.3189/s0260305500004092).
- Cuffey KM and 8 others** (2016) Deglacial temperature history of West Antarctica. *Proceedings of the National Academy of Sciences* **113**(50) 14249–14254. doi: [10.1073/pnas.1609132113](https://doi.org/10.1073/pnas.1609132113).
- Cuffey KM and Steig EJ** (1998) Isotopic diffusion in polar firn: implications for interpretation of seasonal climate parameters in ice-core records, with emphasis on central Greenland. *Journal of Glaciology* **44**(147), 273–284.
- Dahl Jensen D and 6 others** (1998) Past temperatures directly from the Greenland ice sheet. *Science* **282**(5387), 268–271.
- Ellehöj MD, Steen-Larsen HC, Johnsen SJ and Madsen MB** (2013) Ice-vapor equilibrium fractionation factor of hydrogen and oxygen isotopes: experimental investigations and implications for stable water isotope studies. *Rapid Communications in Mass Spectrometry* **27**(19), 2149–2158.
- Emanuelsson BD, Baisden WT, Bertler NAN, Keller ED and Gkinis V** (2015) High-resolution continuous-flow analysis setup for water isotopic measurement from ice cores using laser spectroscopy. *Atmospheric Measurement Techniques* **8**(7), 2869–2883.
- EPICA Community Members** (2004) Eight glacial cycles from an Antarctic ice core. *Nature* **429**(6992), 623–628.
- EPICA Community Members** (2006) One-to-one coupling of glacial climate variability in Greenland and Antarctica. *Nature* **444**(7116) 195–198, ISSN 1476-4687. doi: [10.1038/nature05301](https://doi.org/10.1038/nature05301).
- Fudge TJ and 8 others** (2016) Variable relationship between accumulation and temperature in West Antarctica for the past 31 000 years. *Geophysical Research Letters* **43**(8) 3795–3803.
- Fujita K and Abe O** (2006) Stable isotopes in daily precipitation at Dome Fuji, East Antarctica. *Geophysical Research Letters* **33**(18), L18503–L18503.
- Gkinis V** (2011) *High Resolution Water Isotope Data from Ice Cores* (Ph.D. thesis). Niels Bohr Institute, University of Copenhagen.
- Gkinis V and 6 others** (2011) Water isotopic ratios from a continuously melted ice core sample. *Atmospheric Measurement Techniques* **4**(11), 2531–2542. doi: [10.5194/amt-4-2531-2011](https://doi.org/10.5194/amt-4-2531-2011).
- Gkinis V, Simonsen SB, Buchardt SL, White JWC and Vinther BM** (2014) Water isotope diffusion rates from the NorthGRIP ice core for the last 16 000 years – Glaciological and paleoclimatic implications. *Earth and Planetary Science Letters* **405**(0), 132–141. doi: [10.1016/j.epsl.2014.08.022](https://doi.org/10.1016/j.epsl.2014.08.022).
- Goujon C, Barnola JM and Ritz C** (2003) Modeling the densification of polar firn including heat diffusion: application to close-off characteristics and gas isotopic fractionation for Antarctica and Greenland sites. *JGR: Atmospheres* **108**(D24), 4792–4792.
- Hall WD and Pruppacher HR** (1976) Survival of ice particles falling from cirrus clouds in subsaturated air. *Journal of the Atmospheric Sciences* **33**(10), 1995–2006.

- Herron MM and Langway C** (1980) Firn densification – an empirical-model. *Journal of Glaciology* **25**(93), 373–385.
- Holme C and 7 others** (2019) Varying regional $\delta^{18}\text{O}$ -temperature relationship in high-resolution stable water isotopes from east Greenland. *Climate of the Past* **15**(3), 893–912. doi: [10.5194/cp-15-893-2019](https://doi.org/10.5194/cp-15-893-2019).
- Holme C, Gkinis V and Vinther BM** (2018) Molecular diffusion of stable water isotopes in polar firn as a proxy for past temperatures. *Geochimica et Cosmochimica Acta* **225**, 128–145.
- Jean-Baptiste P, Jouzel J, Stievenard M and Ciais P** (1998) Experimental determination of the diffusion rate of deuterated water vapor in ice and application to the stable isotopes smoothing of ice cores. *Earth and Planetary Science Letters* **158**(1–2), 81–90.
- Johnsen SJ** (1977) Stable isotope homogenization of polar firn and ice. *Isotopes and Impurities in Snow and Ice* 210–219.
- Johnsen SJ and 6 others** (2000) *Diffusion of Stable Isotopes in Polar Firn and Ice. The Isotope Effect in Firn Diffusion*. Sapporo: Hokkaido University Press, pp. 121–140.
- Johnsen SJ and 8 others** (2001) Oxygen isotope and palaeotemperature records from six Greenland ice-core stations: camp Century, Dye-3, GRIP, GISP2, Renland and NorthGRIP. *Journal Of Quaternary Science* **16** (4), 299–307.
- Johnsen SJ and Andersen N** (1978) On power estimation in maximum entropy spectral analysis. *Geophysics* **43**(4), 681–690.
- Johnsen SJ, Dahl Jensen D, Dansgaard W and Gundestrup N** (1995) Greenland paleotemperatures derived from GRIP bore hole temperature and ice core isotope profiles. *Tellus Series B-Chemical And Physical Meteorology* **47**(5), 624–629.
- Jones TR and 7 others** (2017a) Water isotope diffusion in the WAIS divide ice core during the Holocene and last glacial. *Journal of Geophysical Research. Earth Surface* **122**(1), 290–309. doi: [10.1002/2016JF003938](https://doi.org/10.1002/2016JF003938).
- Jones TR and 7 others** (2017b) Improved methodologies for continuous-flow analysis of stable water isotopes in ice cores. *Atmospheric Measurement Techniques* **10**(2), 617–632.
- Jones TR and 5 others** (2018) Southern Hemisphere climate variability forced by Northern Hemisphere ice-sheet topography. *Nature* **554**, 351–355.
- Kahle EC, Holme C, Jones TR, Gkinis V and Steig EJ** (2018) A generalized approach to estimating diffusion length of stable water isotopes from ice-core data. *Journal of Geophysical Research. Earth Surface* **123**(10), 2377–2391. doi: [10.1029/2018JF004764](https://doi.org/10.1029/2018JF004764).
- Kaspers KA and 5 others** (2004) Model calculations of the age of firn air across the Antarctic continent. *Atmospheric Chemistry and Physics* **4**(5), 1365–1380.
- Kreyszig E** (2006) *Advanced Engineering Mathematics*. Hoboken, N.J.: John Wiley & Sons Inc.
- Laepple T and 5 others** (2018) On the similarity and apparent cycles of isotopic variations in East Antarctic snow pits. *The Cryosphere* **12**(1), 169–187.
- Lamb KD and 6 others** (2017) Laboratory measurements of HDO/H₂O isotopic fractionation during ice deposition in simulated cirrus clouds. *Proceedings of the National Academy of Sciences* **114**(22), 5612–5617.
- Li J, Wang WL and Zwally J** (2002) Interannual variations of shallow firn temperature at Greenland summit. *Annals of Glaciology* **35**, 368–370.
- Ligtenberg SRM, Helsen MM, van den Broeke MR** (2011) An improved semi-empirical model for the densification of Antarctic firn. *Cryosphere* **5** (4), 809–819. doi: [10.5194/tc-5-809-2011](https://doi.org/10.5194/tc-5-809-2011).
- Lundin JMD and 12 others** (2017) Firn model intercomparison experiment (FirnMICE). *Journal of Glaciology* **63**(239), 401–422, ISSN 0022-1430. doi: [10.1017/jog.2016.114](https://doi.org/10.1017/jog.2016.114).
- Majoube M** (1971) Fractionation factor of ^{18}O between water vapor and ice. *Journal De Chimie Physique Et De Physico-Chimie Biologique* **68** (4), 625–625.
- Martinier P, Raynaud D, Etheridge DM, Barnola JM and Mazaudier D** (1992) Physical and climatic parameters which influence the air content in polar ice. *Earth and Planetary Science Letters* **112**(1), 1–13.
- Masson-Delmotte V and 22 others** (2015) Recent changes in north-west Greenland climate documented by NEEM shallow ice core data and simulations, and implications for past-temperature reconstructions. *The Cryosphere* **9**(4), 1481–1504.
- Merlivat L** (1978) Molecular diffusivities of H₂¹⁶O, HD¹⁶O, and H₂¹⁸O gases. *Journal of Chemical Physics* **69**(6), 2864–2871. doi: [10.1063/1.436884](https://doi.org/10.1063/1.436884).
- Merlivat L and Nief G** (1967) Fractionnement isotopique lors des changements de état solide-vapeur et liquide-vapeur de leau a des temperatures inferieures a 0 degrees c. *Tellus* **19**(1), 122–127.
- Murphy DM and Koop T** (2005) Review of the vapour pressures of ice and supercooled water for atmospheric applications. *Quarterly Journal of the Royal Meteorological Society* **131**(608), 1539–1565.
- NEEM Community Members** (2013) Eemian interglacial reconstructed from a Greenland folded ice core. *Nature* **493**(7433), 489–494. doi: [10.1038/nature11789](https://doi.org/10.1038/nature11789).
- Nielsen LT, Adalgeirsdóttir G, Gkinis V, Nuterman R and Hvidberg CS** (2018) The effect of a Holocene climatic optimum on the evolution of the Greenland ice sheet during the last 10 kyr. *Journal of Glaciology* **64** (245), 477–488.
- Oerter H, Graf W, Meyer H and Wilhelms F** (2004) The EPICA ice core from Dronning Maud Land: first results from stable-isotope measurements. *Annals of Glaciology*, **39**, 307–312.
- PAGES 2k Consortium** (2013) Continental-scale temperature variability during the past two millennia. *Nature Geoscience* **6**(5), 339–346. doi: [10.1038/ngeo1797](https://doi.org/10.1038/ngeo1797).
- Patankar SV** (1980) *Numerical Heat Transfer and Fluid Flow*. New York: Hemisphere Publishing Corporation (CRC Press, Taylor & Francis Group).
- Press WH, Teukolsky SA, Vetterling WT and Flannery BP** (2007) *Numerical Recipes: The Art of Scientific Computing*. New York: Cambridge University Press.
- Schlosser E and 9 others** (2017) The influence of the synoptic regime on stable water isotopes in precipitation at Dome C, East Antarctica. *The Cryosphere* **11**(5), 2345–2361. doi: [10.5194/tc-11-2345-2017](https://doi.org/10.5194/tc-11-2345-2017).
- Schwander J** (1989) The transformation of snow to ice and the occlusion of gases. *Environmental Record in Glaciers and Ice Sheets* **8**, 53–67.
- Schwander J, Stauffer B and Sigg A** (1988) Air mixing in firn and the age of air at pore close-off. *Annals of Glaciology* **10**, 141–145.
- Simonsen SB and 5 others** (2011) Past surface temperatures at the NorthGRIP drill site from the difference in firn diffusion of water isotopes. *Climate of the Past* **7**(4), 1327–1335. doi: [10.5194/cp-7-1327-2011](https://doi.org/10.5194/cp-7-1327-2011).
- Stenni B and 14 others** (2010) The deuterium excess records of EPICA Dome C and Dronning Maud Land ice cores (East Antarctica). *Quaternary Science Reviews* **29**(1–2), 146–159. doi: [10.1016/j.quascirev.2009.10.009](https://doi.org/10.1016/j.quascirev.2009.10.009).
- Stevens CD** (2018) *Investigations of Physical Processes in Polar Firn through Modeling and Field Measurements* (Ph.D. thesis). University of Washington.
- Stevens CM and 6 others** (2020) The Community Firn Model (CFM) v1.0. *Geoscientific Model Development* **13**(9), 4355–4377. doi: [10.5194/gmd-13-4355-2020](https://doi.org/10.5194/gmd-13-4355-2020).
- Svensson A and 15 others** (2015) On the occurrence of annual layers in Dome Fuji ice core early Holocene ice. *Climate of the Past* **11**(9), 1127–1137. doi: [10.5194/cp-11-1127-2015](https://doi.org/10.5194/cp-11-1127-2015).
- Thompson DC** (1969) The coreless winter at Scott Base Antarctica. *Quarterly Journal of the Royal Meteorological Society* **95**(404), 404–404. doi: [10.1002/qj.49709540413](https://doi.org/10.1002/qj.49709540413).
- Uemura R and 5 others** (2012) Ranges of moisture-source temperature estimated from Antarctic ice cores stable isotope records over glacial-interglacial cycles. *Climate of the Past* **8**(3), 1109–1125. doi: [10.5194/cp-8-1109-2012](https://doi.org/10.5194/cp-8-1109-2012).
- Van der Wel LG, Gkinis V, Pohjola VA and Meijer HAJ** (2011) Snow isotope diffusion rates measured in a laboratory experiment. *Journal of Glaciology* **57**(201), 30–38.
- Veres D and 15 others** (2013) The Antarctic ice core chronology (AICC2012): an optimized multi-parameter and multi-site dating approach for the last 120 thousand years. *Climate of the Past* **9**(4), 1733–1748. doi: [10.5194/cp-9-1733-2013](https://doi.org/10.5194/cp-9-1733-2013).
- Vinther BM and 12 others** (2006) A synchronized dating of three Greenland ice cores throughout the Holocene. *JGR: Atmospheres* **111**(D13), D13102–D13102.
- Vinther BM and 6 others** (2010) Climatic signals in multiple highly resolved stable isotope records from Greenland. *Quaternary Science Reviews* **29**(3–4), 522–538.
- WAIS Divide Project Members** (2015) Precise inter-polar phasing of abrupt climate change during the last ice age. *Nature* **520**(7549), 661–665.

Appendix A: Additional plots and tables

See Figs 20–22 and Table 6.

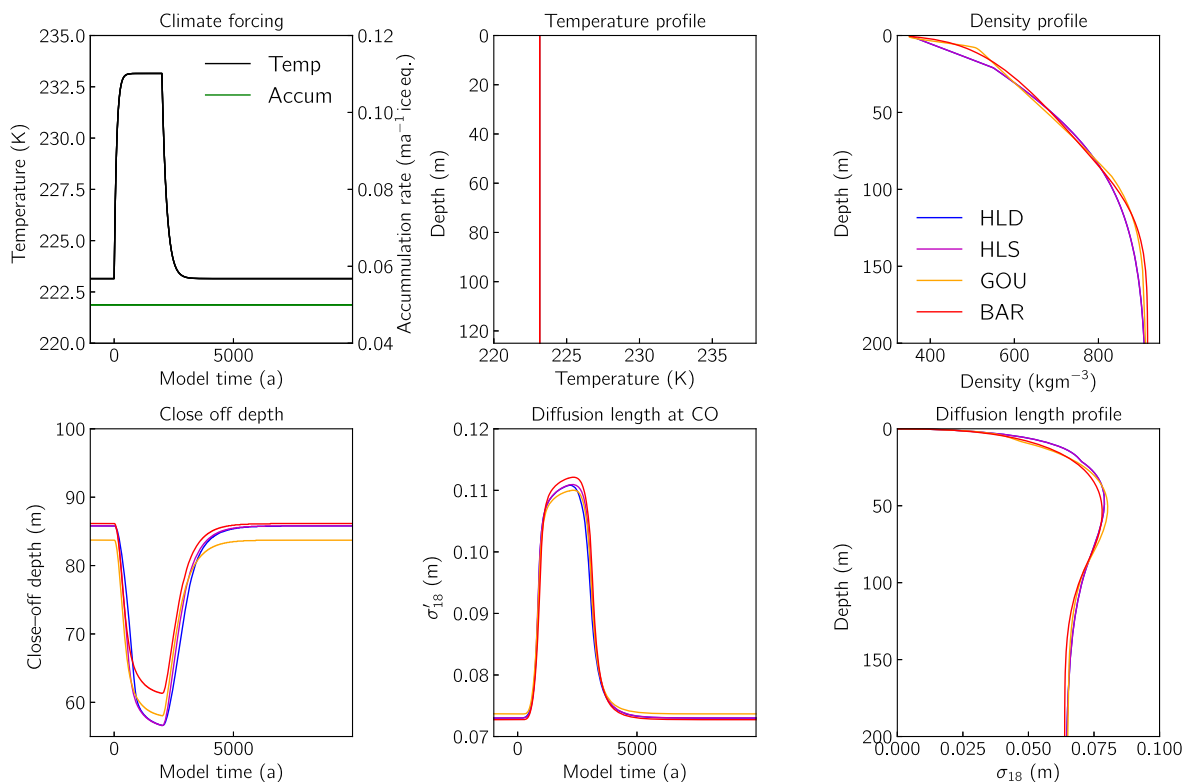


Fig. 20. Model comparison for the warming pulse experiments for $\psi = 100$ years with constant accumulation. The vertical profiles (temperature, density and diffusion length) refer to $t = 10\,000$ years.

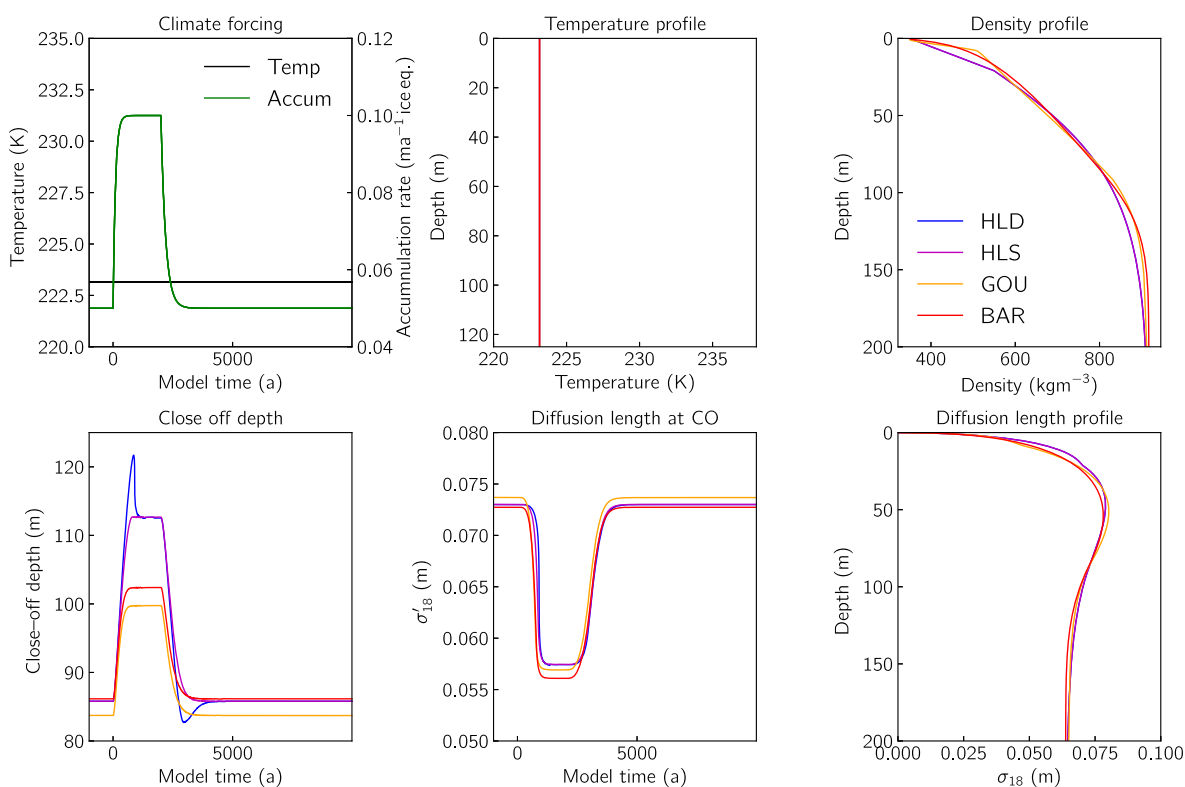


Fig. 21. Model comparison for the warming pulse experiments for $\psi = 100$ years with constant temperature. The vertical profiles (temperature, density and diffusion length) refer to $t = 10\,000$ years.

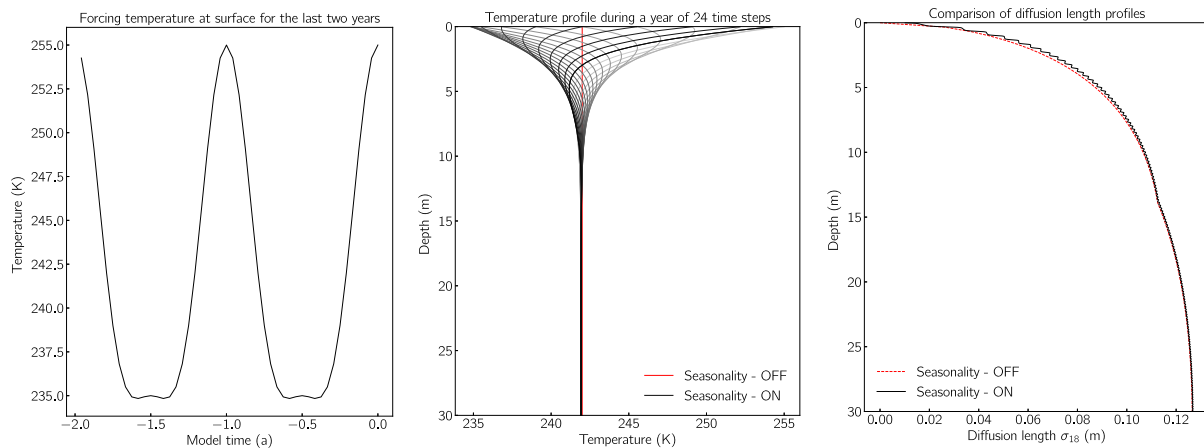


Fig. 22. Steady-state type 2 forcing model run with seasonality ON and OFF. The seasonality amplitude is 10 K. (a) Temperature forcing for type 2 steady-state conditions. We plot the last 2 years of the simulation. Each year has a 24 steps resolution. (b) Temperature profile of the firn column with seasonality OFF (red curve) and ON (grey/black lines). We plot the last 24 time steps of the simulation equivalent of 1 year model time. (c) The diffusion length profile comparison.

Table 6. List of used symbols

Symbol	Unit	Description
A	m a^{-1}	Annual accumulation
b_t	–	Firn tortuosity scaling factor
D	$\text{m}^2 \text{s}^{-1}$	Firn isotope diffusivity
D_a	$\text{m}^2 \text{s}^{-1}$	Diffusivity of water vapour in air
$D_{\text{O}^{18}\text{O}}$	$\text{m}^2 \text{s}^{-1}$	Diffusivity in air for O18
$D_{\text{D}^2\text{H}}$	$\text{m}^2 \text{s}^{-1}$	Diffusivity in air for Deuterium
\hat{G}	m^{-1}	Gaussian filter
\tilde{G}	–	Transfer function of the diffusion process
$k(T)$	–	H-L model temperature dependency Arrhenius function
m	kg	Molecular weight
p	Pa	Saturation vapour pressure over ice
P	Atm	Atmospheric pressure
P_0	Atm	Standard atmospheric pressure
R	$\text{m}^2 \text{Pa K}^{-1} \text{mol}^{-1}$	Molar gas constant
s	–	Total porosity
S	–	Ice thinning
s_{cl}	–	Closed porosity
t	s	Time
T	K	Temperature
T_0	K	Standard temperature
T_{amp}	K	Annual amplitude of temperature
z	m	Depth
$\alpha_{\text{s/v}}^i$	–	Fractionation factor solid over vapour for species i
Γ_A	‰	Magnitude of the annual isotopic signal
Γ_{A0}	‰	Initial magnitude of the annual isotopic signal
δ	‰	Isotopic composition
δ_0	‰	Initial isotopic profile
ϵ_z	s^{-1}	Strain rate
θ	–	H-L model accumulation dependence
λ	m	Wavelength of the isotopic signal
λ_A	m	Wavelength of the annual component in the isotopic signal
ρ	kg m^{-3}	Density
ρ_0	kg m^{-3}	Surface density
ρ_c	kg m^{-3}	Critical density at 550 kg m^{-3}
ρ_{co}	kg m^{-3}	Close-off density
ρ_{ice}	kg m^{-3}	Density of ice
σ	m	Diffusion length
σ'	m	Diffusion length at close-off density
τ	–	Firn tortuosity
ψ	years	Time constant for pulse experiments